Title: **Temperature-dependent solid electrolyte interphase (SEI) reactions drive performance in lithium-mediated nitrogen reduction to ammonia.**

Authors: Peter Benedek[1,2], Yamile E. Cornejo-Carrillo[1,2], Alden H. O'Rafferty[1], Valerie A. Niemann[1,2], Sang-Won Lee[1,2], Eric J. McShane[1], Matteo Cargnello[1,2], Adam C. Nielander[2]**, Thomas F. Jaramillo[1,2,3]*

[1]Department of Chemical Engineering, Stanford University, Stanford, CA 94305, United States

[2]SUNCAT Center for Interface Science and Catalysis, SLAC National Accelerator Laboratory, 2575 Sand Hill Road, Menlo Park, CA 94025, United States

*Correspondence: jaramillo@stanford.edu

** Correspondence: anieland@slac.stanford.edu

[3]Lead contact

Keywords: Electrochemical ammonia synthesis, lithium-mediated nitrogen reduction, temperature, solid electrolyte interphase, time evolution, rinsate analysis, electrolyte decomposition

Summary:

The solid electrolyte interphase (SEI) is a vital component to control mass transport and selectivity in the lithium-mediated reduction of N_2 to NH_3 (Li-N_2R). Finding strategies that generate the optimal SEI, a complex network of organic and inorganic species, can potentially improve Li-N_2R performance. Here, we unravel structure-property relationships of the SEI by correlating its composition with the NH_3 faradaic efficiency (FE_{NH3}). By modifying the reaction temperature, we alter electrolyte decomposition reactions and observe changes in the SEI that explain FE_{NH3} trends between electrolyte solvents. We quantify a complex reaction environment at elevated temperatures where SEI formation is counteracted by etching reactions. This tradeoff leads to temporal fluctuations of FE_{NH3}, but the maximal FE_{NH3} can reach up to 40%, the highest value reported for batch cells at ambient pressure, thus far. Our work underscores the potential of novel electrolytes that steer SEI selectivity and, ultimately, improve Li-N_2R performance.

Introduction

With ammonia (NH_3) production projected to pass 200 megatons per year by 2030[1], finding routes to CO_2-neutral NH_3 production is one of the most important challenges towards a transition to sustainable industry. While adaptations to the existing Haber-Bosch infrastructure via the introduction of green H_2 or point-source carbon capture[2,3] can alleviate some of the emissions, the development of alternative techniques to produce renewable NH_3 will be essential. A promising method that could operate under mild conditions is the electrochemical reduction of N_2 for potential decentralized and intermittent production of NH_3, which would allow for selective fertilizer production during peak power generation.

Among the many existing electrically-driven systems that create NH_3[2], the Li-mediated reduction of N_2 (Li-N_2R) is among the most promising.[4] In this reaction, Li metal is electroplated on the cathode substrate and reacts with N_2, breaking the N-N triple bond at ambient temperatures to form a lithium nitride. A proton donor species (e.g., ethanol[5] or phenol[6]) present in the electrolyte decomposes the nitride into NH_3 and Li^+ that can then redeposit back onto the electrode to repeat the cycle again.[7]

Simultaneously, the electroplated Li reacts with the electrolyte to form a complex surface layer, referred to as the *solid electrolyte interphase* (SEI). Residing at the interface between the plated Li and the bulk electrolyte, the SEI plays a key role controlling the transport of reactants and products, controlling transport in the overall Li-N_2R reaction.[8–10]

While it is generally accepted that the appropriate SEI is crucial to achieve high ammonia faradaic efficiencies (FE_{NH3}) during Li-N_2R, there remains much to understand about

how the SEI impacts the reaction. As the SEI in Li-N_2R is a porous heterostructure that contains a mixture of inorganic and organic species that order in crystalline, amorphous, and molecular phases[11–13], it is challenging to disentangle which factors therein (e.g. chemical species, concentrations, thickness, porosity, etc.) guide performance.

One approach to understand contributions from those factors has been to alter the SEI using different electrolyte salts or additives[8,14–17], correlating changes in the electrochemical performance with electrolyte composition and the structure/morphology of the SEI. A common picture has emerged where additives contributing to inorganic species (such as O_2 and H_2O) and fluorinated electrolytes generate inorganic-rich SEIs that lead to a higher FE_{NH3}. In addition, it has been shown through in situ neutron reflectivity[12,18] and cryo-electron microscopy[13] that the proton source greatly impacts the structure of the SEI as it drives Li metal oxidation. The proton source seems to play a key role in creating a porous network that allows for mass transport of protons and N_2.[19] Accordingly, different proton sources have different affinities to remain trapped in the SEI, suggesting that an optimal organic species loading within the SEI exists.[20]

Similar to Li-N_2R, tuning the composition of the SEI has also been explored in Li metal batteries.[21,22] Efforts in the battery field have studied the impacts of changing the temperature, shown to improve battery performance significantly at higher temperature.[23] Higher temperatures tend to favor the growth of inorganic-rich SEIs, while SEIs formed at lower temperatures tend to be thinner and prone to cracking. For Li metal batteries, this means that higher temperatures lead to the formation of a more stable SEI, and thus longer cycle life.

While these trends hold true for Li metal batteries, there are notable differences from the Li-N_2R system that motivate key questions to be studied regarding temperature effects in

the Li-N_2R system. For example, do higher operating temperatures produce more inorganic-rich SEIs in Li-N_2R as well? Is SEI stability temperature dependent? How is the mass transport of gaseous species impacted? Do higher temperatures allow for improved N_2 fixation? Are parasitic reactions in the electrolyte problematic, i.e. how are the proton source, the electrolyte solvent, or the lithium salt affected at higher temperature?

Here, we studied the composition of the SEI as a function of temperature as well as the temporal dynamics of the SEI and how they correlate to performance. We studied the influence of decomposition reactions and correlated our findings to the observed FE_{NH3}. We provide first insights into how elevated temperatures impact FE_{NH3} in a dynamic way, leading to much improved performance under specific conditions. Based on our findings, we then engineered an electrolyte at elevated temperatures that can reach a peak FE_{NH3} of up to 40% during the reaction, the highest reported FE_{NH3} to our knowledge for this batch process at ambient pressure. Our work provides fundamental insight on temperature-dependent processes in Li-N_2R to inform the design of SEIs and maximize Li-N_2R performance.

Results

While a vast parameter space for Li-N_2R electrolyte composition exists[6,7,24], we focused on commonly used electrolytes that contain 1 M lithium tetrafluoroborate ($LiBF_4$) as a salt and ethanol (EtOH) as a proton source (see **Figure 1a**). For the solvent, we studied bis(2-methoxyethyl) ether (diglyme) and tetrahydrofuran (THF). Our temperature studies ranged from 5 °C to 80 °C.

As temperature can impact a great number of chemical and physical factors, we started by measuring changes in the electrolyte conductivity as a function of temperature using

electrochemical impedance spectroscopy (see **Figure 1b**). 1 M $LiBF_4$ in THF maintains a relatively low conductivity of approximately 7 mS cm^{-1} over the studied temperature range. This finding is in line with previous studies, where the strongest $LiBF_4$-solvent interactions were reported in THF[25]. Conversely, the diglyme-based electrolyte shows a substantial temperature dependence of the conductivity, increasing from a value of 15 mS cm^{-1} at 22 °C to 27 mS cm^{-1} at 60 °C. Below room temperature, however, the conductivity decreases substantially, and the formation of a white gel is observed, suggestive of precipitation of $LiBF_4$.

These conductivity trends indicate that overpotentials due to ohmic losses are relatively insensitive to temperature for THF-based electrolytes, while for diglyme-based electrolytes substantial improvement in electrolyte conductivity is observed above room temperatures. Under an applied current density of j = -1 mA cm^{-2} we also found improvements in potential under operation at the Pt anode at temperatures at and above 60 °C (**Figure 1c**). At these temperatures, the observed initial anode potential is more than 0.5 V less positive than the potential at room temperature, suggesting a different oxidation reaction or substantially improved reaction kinetics at the anode as a function of temperature. Interestingly, the steady-state Li plating potential remains largely unaffected by temperature changes at the cathode. However, a substantial change in the reduction behavior occurs before the Li plating potential is reached (**Figure 1c**, inset). With increasing temperature, a larger amount of charge was passed in the voltage range between -1.5 V and -2.5 V vs. $Li_{0.5}FePO_4$.[26] In agreement with previous research[20] and a compositional analysis of the SEI (see **Figure S6**), we attribute this additional charge to an increased amount of SEI species. This is further exemplified by galvanostatic Li-N_2R executed over 4 hours at a current density of -4 mA cm^{-2}, well past the 5-10 mAh cm^{-2} threshold that is required for SEI formation.[20] After isolating and washing the Cu cathode used in the galvanostatic experiment, we observed the formation of SEI deposits on

the electrode that increase in thickness at temperatures up to 50 °C (see **Figure 1d** and **Figure S7**). In addition, the SEI layer became qualitatively more brittle above 40 °C, leading to cracks and the detachment of the SEI; after severe detachment at 80 °C, the SEI that is left behind is no longer clearly visible. We also observed that higher temperatures lead to a more porous SEI, with SEI particle sizes in the range of 1 μm and SEI thicknesses from a few micrometers to beyond 50 μm (see electron microscopy images of SEI cross sections in **Figure S8**).

We evaluated the species composition in the SEI using a rinsing method to separate the washed SEI from the electrode, followed by analysis via nuclear magnetic resonance (NMR), inductively coupled plasma mass spectrometry (ICP-MS), and ion chromatography (IC); these methods were used to quantify the mass of organic species (NMR), lithium and boron (ICP-MS), and fluoride (IC), respectively. In line with the visual observations, we saw a strong increase in the mass of SEI deposits from 4 mg cm^{-2} at room temperature to 14 mg cm^{-2} at 50 °C for diglyme-based electrolytes (**Figure 2a**). Assuming that the mass density of the SEI composite is in the range of 1-2 g/cm^3 and porosities between 0-50 %, this amounts to approximate SEI thicknesses in the range of 20 to 80 μm at room temperature and 70 to 280 μm at 50 °C. Above 50 °C, the mass of SEI deposits starts dropping until only approximately 2 mg cm^{-2} of the deposits remain at 80 °C. Remarkably, contrary to earlier studies in fluorinated electrolytes from Li ion batteries[27], the ratio between organic and inorganic species remains largely independent of temperature. We hypothesize that this is due to the high boiling point and viscosity of diglyme which leads to electrolyte entrapment in the porous structure of the SEI.[28]

The mass of the SEI species in the THF-based electrolyte followed a similar trend as the diglyme-based electrolyte, within its temperature range of operation (see **Figure 2b**). We observed a constant increase of the SEI species mass with increasing temperature, until 40 °C,

at which point the SEI becomes irregular (see **Figure S7**). The SEI, however, is almost solely composed of lithium and fluorides. This is in contrast to previous findings with $LiClO_4$ based electrolytes, in which case a buildup of organic species was observed.[20] We hypothesize that, as fluorinated electrolyte salts decompose to a much more uniform SEI than $LiClO_4$[14], much of the organic outer SEI layer remains accessible to THF and ends up dissolved in the electrolyte rather than being deposited. Furthermore, THF coordination leads to a stabilization of B-F bonds in $LiBF_4$[25], hence reducing the boron build up in the SEI.

The changes in SEI composition were correlated with changes in the Li-N_2R selectivity to NH_3 (**Figure 2c**).[29] FE_{NH3} stays approximately constant over a temperature range of 25 °C to 50 °C for diglyme and 5 °C to 25 °C for THF. Above these temperatures, FE_{NH3} drops precipitously. Furthermore, FE_{NH3} for diglyme is significantly higher over the entire temperature range, with a maximum of 13(+/- 2) %, whereas FE_{NH3} is 5(+/- 1) % for THF. We note that under lower total passed charge conditions (2 mAh cm^{-2}), FE_{NH3} in diglyme-based electrolytes increased with increasing temperature as more SEI formed (see **Figure S6**), underscoring the importance of running Li-N_2R experiments beyond the charge passed for SEI formation.[20]

Our findings in SEI composition with diglyme- and THF-based electrolytes highlight a complex relationship between SEI composition and FE_{NH3}. Despite the threefold increase in SEI mass observed with diglyme-based electrolyte between 25 °C and 50 °C, which one would assume to impede mass transport and be detrimental to Li-N_2R performance, FE_{NH3} in diglyme-based electrolytes remains approximately constant. We hypothesize that high porosity induced by organic species together with enhanced Li reactivity at higher temperatures limits the loss of FE_{NH3} due to the SEI mass increase. This is supported by FIB-SEM cross sections (see

Figure S8), where we observed a large porous network with pore sizes in the micrometer range. In turn, the THF-based electrolyte does not contain many organic species, leading to an accumulation of a dense LiF layer that might impede N_2 transport enough, that FE_{NH3} drops upon SEI build up. We indeed found via a current-cycling method (see **Supplementary Note 1**) that the THF-based SEI passivated the cathode surface more than the diglyme-based SEI, suggesting the generation of such a dense layer. Furthermore, depth-resolved x-ray photoemission spectroscopy (XPS) measurements showed that the carbon amount in the THF-based SEI decreased strongly in deeper levels of the SEI, while remaining approximately constant for diglyme (see **Figure S12-S14**). Our findings are also consistent with previous studies that have shown the importance of ethoxides to facilitate pore formation within the SEI.[13]

Another interesting observation is the loss of SEI at elevated temperatures, i.e., above 50 °C for diglyme-based and 40 °C for THF-based electrolytes, respectively. This reduction in the observed mass of SEI was correlated with defects observed in the SEI films and color changes of the Cu working electrode (**Figure S15**); we view these observations to be consistent with chemical etching and delamination processes that occur at the electrode surface at elevated temperatures. As the SEI develops a thickness in the range of 100 µm at those elevated temperatures, it is likely that any etching reaction that would occur at the interface between SEI and Cu results in delamination of the SEI. Indeed, when studying Cu etching under open-circuit conditions via ICP-MS in solutions of 1 M $LiBF_4$ in THF, diglyme, or EtOH, respectively, we observe an increase of the Cu etch rate at elevated temperatures (see **Figure 3a**). Substantial etching is observed in EtOH, with etch rates increasing from < 0.1 µg/min at room temperature up to 10 µg/min at 80 °C. In contrast, very limited (< 1 µg/min) Cu etching is observed in THF and diglyme, pointing towards higher reactivity of hydroxyl groups. We hence hypothesize that $LiBF_4$ in the presence of EtOH etches the electrode surface — this may

be via direct etching or through a $LiBF_4$ decomposition reaction[11] that forms boron trifluoride (BF_3). BF_3 can subsequently react with ethanol to form triethyl borate and hydrofluoric acid (HF) as side product (see **Figure 3b**). We detected these borate moieties via XPS (see **Figure S12-S14**) and ^{11}B NMR measurements (see **Figure S16**). ^{11}B NMR measurements also suggest the appearance of BF_3 in the SEI rinsate.[30,31] Note, that even high purity, commercial THF contains difficult-to-remove alcohol impurities[19], which may explain the higher Cu etch rate (see **Figure 3a**) and the lower onset temperature for SEI dissolution. Furthermore, when we studied Cu etching under Li-N_2R conditions in the diglyme-based electrolyte at early stages of SEI formation (i.e., after 2 mAh cm^{-2} charge was passed at a current density of -1 mA cm^{-2}), we found that the mass of etched Cu is reduced above 50 °C (see **Figure S6**). Simultaneously, the mass of SEI species plateaued at these temperatures, suggesting that not only Cu but also SEI species are etched.

The etching that occurs at the electrode surface during operation presents the possibility of a remarkably dynamic interface. First, at early stages of the reaction, one could expect a steady buildup of the SEI commensurate with an increase of FE_{NH3} that reaches a maximum when the SEI is fully formed. Secondly, the SEI formation decelerates with increasing passivation[32], and at some point it becomes possible for the interface etching rate to take over and cause a drop in FE_{NH3}. Finally, as the SEI becomes less passivated due to etching, the SEI layer can then have an opportunity to rebuild itself over time, reversing the FE_{NH3} drop. This interplay between the rates of etching and SEI rebuild could be cyclical, causing fluctuations of FE_{NH3}.

To test this hypothesis, we took periodic aliquots during the Li-N_2R reaction in diglyme at 25 °C and 50 °C (see **Figure 3c** and **3d**, respectively). As expected at 25 °C, FE_{NH3} is steadily increased until it plateaued at 12% after 4-5 mAh cm^{-2} of charge are passed (**Figure 3c**). At

50 °C, FE_{NH3} increased until reaching a maximum of 18% at 10 mAh/cm^2 after which it dropped below 6% and then rose again to 10-16%, supporting the 'cyclic' hypothesis described above. By tracking the degree of passivation at the cathode (see **Supplementary Note 1**), we observed similar fluctuations in the electrode passivation after 12 mAh/cm^{-2} of passed charge at 50 °C which did not occur at 30 °C, supporting the idea of SEI loss that can lead to fluctuations. Interestingly, while the overall FE_{NH3} for the Li-N_2R runs between 25 °C and 50 °C are within the same range, given that disturbances due to sample retrieval might affect the system performance (see **Figure S2**)[14,33], their dynamic evolution is very different. Particularly, the maximum FE_{NH3} obtained at 50 °C is, with a factor of 1.5, significantly higher than the maximum FE_{NH3} at 25 °C. This result suggests that FE_{NH3} at higher temperature could be significantly higher if there were no etching.

We also aimed to understand the dependence of Li-N_2R performance as a function of initial EtOH content at a temperature of 50 °C after 16mAh cm^{-2} of charge passed (**Figure 4**), where etching and strong SEI growth lead to an initial FE_{NH3} drop, motivating a deeper study of proton transport. Indeed, we observed a convoluted behavior in the SEI growth, where not only EtOH but also all the other SEI species increase in mass up to 1 v% EtOH content, followed by a reduction of SEI species at 1.3 v%.

While the drop in SEI mass was consistent with increased etching at higher proton concentrations, the increase in SEI mass up to 1.0 v% EtOH content was unexpected and suggests that EtOH participates in the buildup of a thick SEI. We hypothesize that higher amounts of EtOH could generate a more porous SEI, that leads to a less passivated Cu electrode (see **Supplementary Note 1**) and consequently result in increased overall SEI growth. The reduction of the SEI mass from 14 mg cm^{-2} to below 4 mg cm^{-2} likely improves mass transport, and we observed that FE_{NH3} showed the same trend as theoretically observed in mass transport

limited Li-N_2R[9,10]. Specifically, in line with proton transport limited behavior, we initially observed an FE_{NH3} increase from ~7(+/- 4)% without EtOH to 19(+/- 1)% with 0.33 v% EtOH content after which FE_{NH3} gradually decreased (**Figure 4b**).

To check whether the reduced proton concentration reduces electrode surface etching, we studied the dynamic evolution of FE_{NH3} during Li-N_2R with 0.33 v% EtOH (**Figure 4c** and **Figure S17**). We still observed fluctuations of FE_{NH3} as a function of charge passed, suggesting the persistence of etching and delamination in solution. Moreover, FE_{NH3} rises to close to 40% for short periods in time, which to our knowledge is the highest FE_{NH3} observed in a batch cell[34] at ambient pressure, thus far (see **Table S7**).[15]

Discussion

The results in this study suggest an interesting tradeoff. In diglyme at higher temperatures, we reach a higher 'instantaneous' FE_{NH3} than at lower temperatures. However, increased etching at higher temperatures can also harm performance, leading to an average FE_{NH3} that is similar to the average FE_{NH3} at lower temperatures. This points to the mitigation of SEI etching as a possible means to enable sustained performance and show unprecedented NH_3 selectivity. One option for mitigation could be the use of HF scavengers that have been successfully employed in Li ion batteries.[35] Alternatively, the replacement of Cu with stainless steel could show promise to reduce the detrimental effects of HF etching. One could also attempt to prevent HF formation altogether by changing either the proton source or the electrolyte salt. This would likely require a new optimization of the SEI formation process that could be readily achieved through the route presented here. For this, our results suggest that the target SEI loading should be in the range of 1 mg cm^{-2} and contain both organic and inorganic species. Once such an electrolyte is found at room temperature, carefully elevating

the temperature while adjusting the proton source content to decrease the overall SEI thickness is a strategy, informed by the study herein, that could potentially increase FE_{NH3}.

We note that these studies were performed in a batch cell with diglyme oxidation as counter electrode reaction. While translating this experiment from batch to flow cell with H_2 oxidation at the anode is generally improving FE_{NH3} due to the favorable mass transport environment in membrane electrode assemblies[4], we anticipate that the electrolyte composition will change under different cell architectures (e.g., flow cell) and anode (e.g., H_2 oxidation) conditions. While we expect that the temperature-driven effects on the SEI layer formation described here can serve as a guideline across these conditions, characterizing the impact of these changes on SEI layer formation and structure is important future work.

Similarly, the $LiBF_4$ decomposition may also be affected by the proton-providing anode reaction. Therefore, we assume that the electrolyte formulation will have to be adapted to account for the oxidation reaction at the anode. We also expect that investigations of metals beyond lithium for this and other metal-mediated reactions could benefit from temperature studies in a similar vein. Given the dynamics of the SEI, for any metal-mediated system understanding the physical and chemical evolution of the SEI with time can inform designs for improved short-term and long-term performance.

Beyond the direct findings, the study presented here enhances our understanding how SEIs guide Li-N_2R performance. Combining SEI composition characterization with FE sampling during Li-N_2R and analytical techniques such as current cycling provides a framework to track the SEI qualitatively with readily accessible tools. It generates a picture of an SEI that impacts the Li-N_2R performance through its dynamic changes. At the same time, we find that the structure of the SEI plays a key role in the eventual performance. If the SEI is too thick, it can impede transport and lead to delamination, while SEIs that are too thin do not passivate the electrode enough and lead to parasitic reactions. In parallel, the composition requires organic

species that allow for porosity and better mass transport. Thus, building the "optimal" SEI will require strategies like the ones shown here that can quantitatively track the species present in the SEI and predict the stability of the cell.

In summary, we have performed a rigorous study on temperature effects on SEI formation and the evolution of FE_{NH3} in Li-N_2R. We find a general degradation of performance in THF-based electrolytes with increasing temperatures, likely due to the formation of a purely inorganic SEI layer that hinders ion and gas transport. In contrast, the performance of diglyme-based electrolytes remains approximately constant up to 50 °C due to the counteracting processes of increased Li-N_2R performance at elevated temperatures and etching of the SEI due to the degradation of the $LiBF_4$ electrolyte salt. This leads to an interesting dynamic evolution of FE_{NH3}, where the interplay between SEI formation and SEI loss caused by etching leads to fluctuations of the FE. By optimizing the ethanol content, we show that a record FE_{NH3} of 40% can be achieved in a batch cell, and our results motivate efforts aimed at mitigating SEI etching as a means to maintain high selectivity and stable performance.

Experimental Procedures

Details regarding experimental procedures can be found under the Experimental Procedures section of the **Supplemental Information**.

Resource Availability

Lead contact

Further information and requests for resources should be directed to and will be fulfilled by the lead contact, Thomas F. Jaramillo (jaramillo@stanford.edu).

Materials Availability

This study did not generate unique new reagents.

Data and Code Availability

The data presented in this work are available from the corresponding authors upon reasonable request.

Acknowledgements

P.B., V.A.N, E.J.M., M.C., and T.F.J. acknowledge primary funding from the Villum foundation's V-SUSTAIN Grant 9455. S.L. acknowledges the Cleantech FWP 100898 funded by the U.S. Department of Energy, Office of Science, Basic Energy Sciences. A.C.N. acknowledges support from the U.S. Department of Energy, Office of Science, Office of Basic Energy Sciences, Chemical Sciences, Geosciences, and Biosciences Division, Catalysis Science Program through the SUNCAT Center for Interface Science and Catalysis. We thank Stephen Lynch for his support for NMR measurements that were performed at Stanford University and supported by the NIH High End Instrumentation grant (1 S10 OD028697-01). Geoff McConohy is acknowledged for the designs of the MAST cell used for air-free scanning electron microscopy measurements, as well as Guangchao Li and the Environmental Measurement Facility staff at Stanford university for their assistance in conducting ion chromatography experiments.

Author contributions

Conceptualization, P.B., V.A.N., A.H.O., M.C., A.C.N., and T.F.J; Methodology, P.B., V.A.N, E.J.M. A.H.O., Y.E.C.C., M.C., A.C.N., and T.F.J; Investigation, P.B., Y.E.C.C., A.H.O., and S.L.; Writing-Original Draft, P.B., A.H.O., V.A.N., S.L., E.J.M., M.C., A.C.N., and T.F.J.; Writing-Review & Editing, P.B., Y.E.C.C., A.H.O., V.A.N., S.L., E.J.M., M.C., A.C.N., and T.F.J.; Funding Acquisition, M.C., A.C.N., and T.F.J.; Supervision: A.C.N., and T.F.J.

Declaration of interests

The authors declare no competing interests

References

(1) IEA. *IEA, Global ammonia production by technology and scenario, 2020-2050*. IEA. Licence: CC BY 4.0. https://www.iea.org/data-and-statistics/charts/global-ammonia-production-by-technology-and-scenario-2020-2050.

(2) Rouwenhorst, K. H. R., Travis, A. S., and Lefferts, L. (2022). 1921–2021: A century of renewable ammonia synthesis. Sustain. Chem. *3*, 149–171. https://doi.org/10.3390/suschem3020011.

(3) Ghavam, S., Vahdati, M., Wilson, I. A. G., and Styring, P. (2021). Sustainable ammonia production processes. Front. Energy Res. *9*, 580808. https://doi.org/10.3389/fenrg.2021.580808.

(4) Fu, X. (2023). Lithium-mediated nitrogen reduction for electrochemical ammonia synthesis: from batch to flow reactor. Mater. Today Catal. *3*, 100031. https://doi.org/10.1016/j.mtcata.2023.100031.

(5) Krishnamurthy, D., Lazouski, N., Gala, M. L., Manthiram, K., and Viswanathan, V. (2021). Closed-loop electrolyte design for lithium-mediated ammonia synthesis. ACS Cent. Sci. *7*, 2073–2082. https://doi.org/10.1021/acscentsci.1c01151.

(6) Fu, X., Xu, A., Pedersen, J. B., Li, S., Sažinas, R., Zhou, Y., Andersen, S. Z., Saccoccio, M., Deissler, N. H., Mygind, J. B. V., et al. (2024). Phenol as proton shuttle and buffer for lithium-mediated ammonia electrosynthesis. Nat. Commun. *15*, 2417. https://doi.org/10.1038/s41467-024-46803-w.

(7) Tsuneto, A., Kudo, A., and Sakata, T. (1994). Lithium-mediated electrochemical reduction of high pressure N_2 to NH_3. J. Electroanal. Chem. *367*, 183–188. https://doi.org/10.1016/0022-0728(93)03025-K.

(8) Katja, L., Z, A. S., J, S. M., Mattia, S., J, B. V., Kevin, K., Rokas, S., B, P. J., Vahid, S., Yuanyuan, Z., et al. (2021). Enhancement of lithium-mediated ammonia synthesis by addition of oxygen. Science *374*, 1593–1597. https://doi.org/10.1126/science.abl4300.

(9) Lazouski, N., Schiffer, Z. J., Williams, K., and Manthiram, K. (2019). Understanding continuous lithium-mediated electrochemical nitrogen reduction. Joule *3*, 1127–1139. https://doi.org/10.1016/j.joule.2019.02.003.

(10) Fu, X., Niemann, V. A., Zhou, Y., Li, S., Zhang, K., Pedersen, J. B., Saccoccio, M., Andersen, S. Z., Enemark-Rasmussen, K., Benedek, P., et al. (2024). Calcium-mediated nitrogen reduction for electrochemical ammonia synthesis. Nat. Mater. *23*, 101–107. https://doi.org/10.1038/s41563-023-01702-1.

(11) Deissler, N. H., Mygind, J. B. V., Li, K., Niemann, V. A., Benedek, P., Vinci, V., Li, S., Fu, X., Vesborg, P. C. K., Jaramillo, T. F., et al. (2024). Operando investigations of the solid electrolyte interphase in the lithium mediated nitrogen reduction reaction. Energy Environ. Sci. *17*, 3482–3492. https://doi.org/10.1039/D3EE04235A.

(12) Blair, S. J., Doucet, M., Niemann, V. A., Stone, K. H., Kreider, M. E., Browning, J. F., Halbert, C. E., Wang, H., Benedek, P., McShane, E. J., et al. (2023). Combined, time-resolved, in situ neutron reflectometry and x-ray diffraction analysis of dynamic SEI formation during electrochemical N_2 reduction. Energy Environ. Sci. *16*, 3391–3406. https://doi.org/10.1039/D2EE03694K.

(13) Steinberg, K., Yuan, X., Klein, C. K., Lazouski, N., Mecklenburg, M., Manthiram, K., and Li, Y. (2022). Imaging of nitrogen fixation at lithium solid electrolyte interphases via cryo-electron microscopy. Nat. Energy *8*, 138–148. https://doi.org/10.1038/s41560-022-01177-5.

(14) Li, S., Zhou, Y., Li, K., Saccoccio, M., Sažinas, R., Andersen, S. Z., Pedersen, J. B., Fu, X., Shadravan, V., Chakraborty, D., et al. (2022). Electrosynthesis of ammonia with

high selectivity and high rates via engineering of the solid-electrolyte interphase. Joule *6*, 2083–2101. https://doi.org/10.1016/j.joule.2022.07.009.

(15) Spry, M., Westhead, O., Tort, R., Moss, B., Katayama, Y., Titirici, M.-M., Stephens, I. E. L., and Bagger, A. (2023). Water increases the faradaic selectivity of li-mediated nitrogen reduction. ACS Energy Lett. *8*, 1230–1235. https://doi.org/10.1021/acsenergylett.2c02792.

(16) Lim, C., Kim, D., Kim, M., Yun, H., Shin, D., Hwang, Y. J., Shin, H., and Yong, K. (2023). Effect of sulfur-derived solid electrolyte interphase on li-mediated nitrogen reduction. ACS Energy Lett. *8*, 4875–4884. https://doi.org/10.1021/acsenergylett.3c02038.

(17) Du, H.-L., Chatti, M., Hodgetts, R. Y., Cherepanov, P. V, Nguyen, C. K., Matuszek, K., MacFarlane, D. R., and Simonov, A. N. (2022). Electroreduction of nitrogen with almost 100% current-to-ammonia efficiency. Nature *609*, 722–727. https://doi.org/10.1038/s41586-022-05108-y.

(18) Blair, S. J., Doucet, M., Browning, J. F., Stone, K., Wang, H., Halbert, C., Avilés Acosta, J., Zamora Zeledón, J. A., Nielander, A. C., Gallo, A., et al. (2022). Lithium-mediated electrochemical nitrogen reduction: tracking electrode–electrolyte interfaces via time-resolved neutron reflectometry. ACS Energy Lett. *7*, 1939–1946. https://doi.org/10.1021/acsenergylett.1c02833.

(19) Valbæk Mygind, J. B., Pedersen, J. B., Li, K., Deissler, N. H., Saccoccio, M., Fu, X., Li, S., Sažinas, R., Andersen, S. Z., Enemark-Rasmussen, K., et al. (2023). Is ethanol essential for the lithium-mediated nitrogen reduction reaction? ChemSusChem *16*, e202301011. https://doi.org/10.1002/cssc.202301011.

(20) McShane, E. J., Niemann, V. A., Benedek, P., Fu, X., Nielander, A. C., Chorkendorff, I., Jaramillo, T. F., and Cargnello, M. (2023). Quantifying influence of the solid-electrolyte

interphase in ammonia electrosynthesis. ACS Energy Lett. *8*, 4024–4032. https://doi.org/10.1021/acsenergylett.3c01534.

(21) Wu, H., Jia, H., Wang, C., Zhang, J., and Xu, W. (2021). Recent progress in understanding solid electrolyte interphase on lithium metal anodes. Adv. Energy Mater. *11*, 2003092. https://doi.org/10.1002/aenm.202003092.

(22) Jurng, S., Brown, Z. L., Kim, J., and Lucht, B. L. (2018). Effect of electrolyte on the nanostructure of the solid electrolyte interphase (SEI) and performance of lithium metal anodes. Energy Environ. Sci. *11*, 2600–2608. https://doi.org/10.1039/C8EE00364E.

(23) Wang, J., Huang, W., Pei, A., Li, Y., Shi, F., Yu, X., and Cui, Y. (2019). Improving cyclability of li metal batteries at elevated temperatures and its origin revealed by cryo-electron microscopy. Nat. Energy *4*, 664–670. https://doi.org/10.1038/s41560-019-0413-3.

(24) Cai, X., Li, X., You, J., Yang, F., Shadike, Z., Qin, S., Luo, L., Guo, Y., Yan, X., Shen, S., et al. (2023). Lithium-mediated ammonia electrosynthesis with ether-based electrolytes. J. Am. Chem. Soc. *145*, 25716–25725. https://doi.org/10.1021/jacs.3c08965.

(25) Seo, D. M., Boyle, P. D., Allen, J. L., Han, S.-D., Jónsson, E., Johansson, P., and Henderson, W. A. (2014). Solvate structures and computational/spectroscopic characterization of $LiBF_4$ electrolytes. J. Phys. Chem. *C 118*, 18377–18386. https://doi.org/10.1021/jp5046782.

(26) McShane, E. J., Benedek, P., Niemann, V. A., Blair, S. J., Kamat, G. A., Nielander, A. C., Jaramillo, T. F., and Cargnello, M. (2023). A versatile $Li_{0.5}FePO_4$ reference electrode for nonaqueous electrochemical conversion technologies. ACS Energy Lett. *8*, 230–235. https://doi.org/10.1021/acsenergylett.2c02190.

(27) Andersson, A. M., and Edström, K. (2001). Chemical composition and morphology of the elevated temperature SEI on graphite. J. Electrochem. Soc. *148*, A1100. https://doi.org/10.1149/1.1397771.

(28) Sauter, C., Zahn, R., and Wood, V. (2020). Understanding electrolyte infilling of lithium ion batteries. J. Electrochem. Soc. *167*, 100546. https://doi.org/10.1149/1945-7111/ab9bfd.

(29) Nielander, A. C., McEnaney, J. M., Schwalbe, J. A., Baker, J. G., Blair, S. J., Wang, L., Pelton, J. G., Andersen, S. Z., Enemark-Rasmussen, K., Čolić, V., et al. (2019). A versatile method for ammonia detection in a range of relevant electrolytes via direct nuclear magnetic resonance techniques. ACS Catal. *9*, 5797–5802. https://doi.org/10.1021/acscatal.9b00358.

(30) Eisele, L., Laszczynski, N., Görg, M., Schneider, M., Burger, S., Radkte, V., Lucht, B., and Krossing, I. (2020). Investigation of mixtures of BF_3 carbonates and LiX (X = OCH_2CF_3, $OC(H)(CF_3)_2$, CO_2CF_3) as novel electrolyte systems for lithium ion batteries. J. Electrochem. Soc. *167*, 080507. https://doi.org/10.1149/1945-7111/ab8876.

(31) Parimalam, B. S., and Lucht, B. L. (2018). Reduction reactions of electrolyte salts for lithium ion batteries: $LiPF_6$, $LiBF_4$, LiDFOB, LiBOB, and LiTFSI. J. Electrochem. Soc. *165*, A251. https://doi.org/10.1149/2.0901802jes.

(32) Müller, S., Pietsch, P., Brandt, B.-E., Baade, P., De Andrade, V., De Carlo, F., and Wood, V. (2018). Quantification and modeling of mechanical degradation in lithium-ion batteries based on nanoscale imaging. Nat. Commun. *9*, 2340. https://doi.org/10.1038/s41467-018-04477-1.

(33) Benedek, P., Wenzler, N., Yarema, M., and Wood, V. C. (2017). Low temperature hydrothermal synthesis of battery grade lithium iron phosphate. RSC Adv. *7*, 17763–17767. https://doi.org/10.1039/C7RA00463J.

(34) Chang, W., Jain, A., Rezaie, F., and Manthiram, K. (2024). Lithium-mediated nitrogen reduction to ammonia via the catalytic solid–electrolyte interphase. Nat. Catal. *7*, 231–241.. https://doi.org/10.1038/s41929-024-01115-6.

(35) Han, J.-G., Jeong, M.-Y., Kim, K., Park, C., Sung, C. H., Bak, D. W., Kim, K. H., Jeong, K.-M., and Choi, N.-S. (2020). An electrolyte additive capable of scavenging HF and PF_5 enables fast charging of lithium-ion batteries in $LiPF_6$-based electrolytes. J. Power Sources *446*, 227366. https://doi.org/10.1016/j.jpowsour.2019.227366.

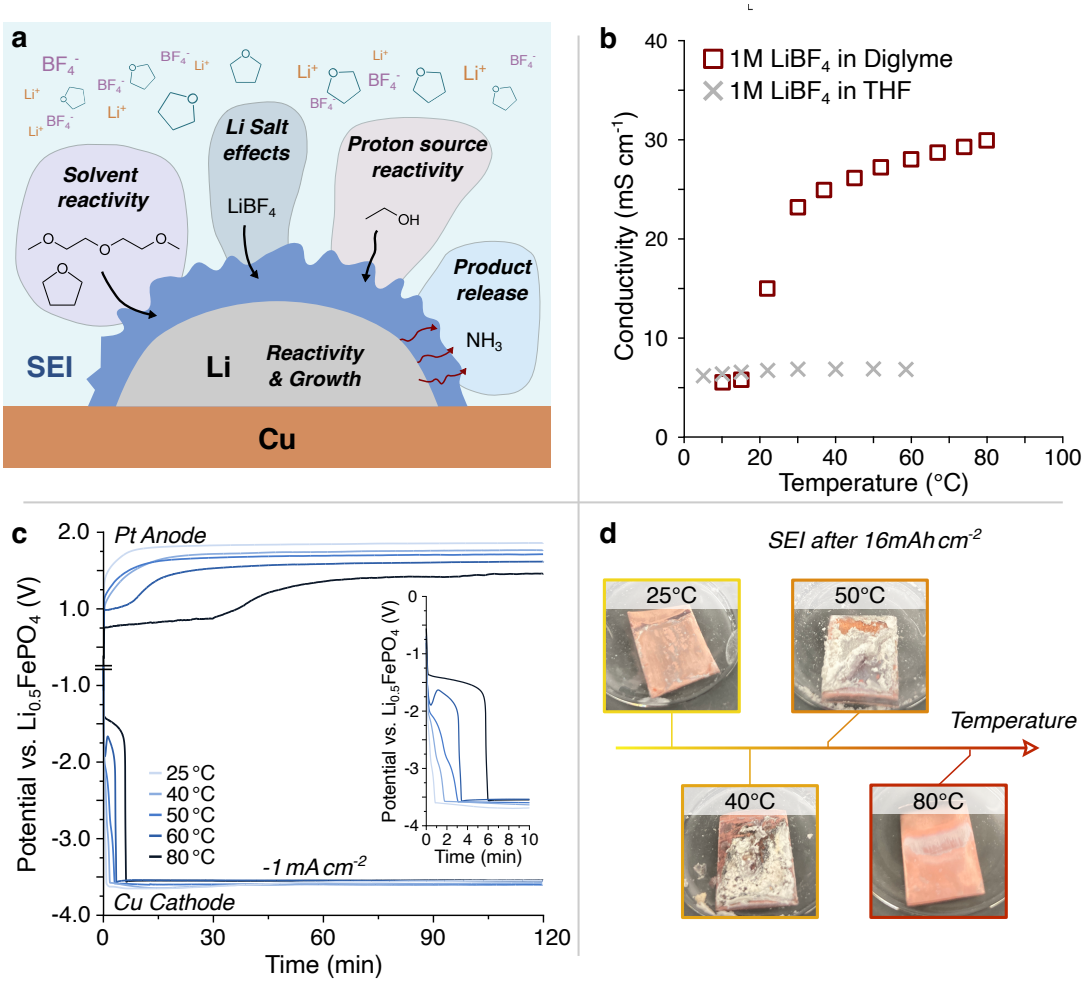

Figure 1. Electrochemical Analysis of temperature dependence during Li-N_2R.

a) Schematic drawing of electrochemical system parameters that play a role in solid electrolyte interphase (SEI) formation. The highlighted parameters were analyzed in this study. **b)** Conductivity of diglyme- and THF-based electrolytes as a function of temperature measured by electrochemical impedance spectroscopy. In both cases, the electrolyte contains 1 M $LiBF_4$ and 1 vol% of EtOH are added. Due to the low boiling point of THF (66 °C), conductivity measurements were only performed up to 60 °C for the THF-based electrolyte. **c)** Voltage profile of Li-N_2R as a function of temperature. During the experiment, a constant current density of -1 mA cm^{-2} was applied to the working electrode in 1M $LiBF_4$ in diglyme. **d)** Photographs of the washed and dried Cu cathodes after 16 mAh cm^{-2} of applied charge at different temperatures with diglyme as the electrolyte solvent.

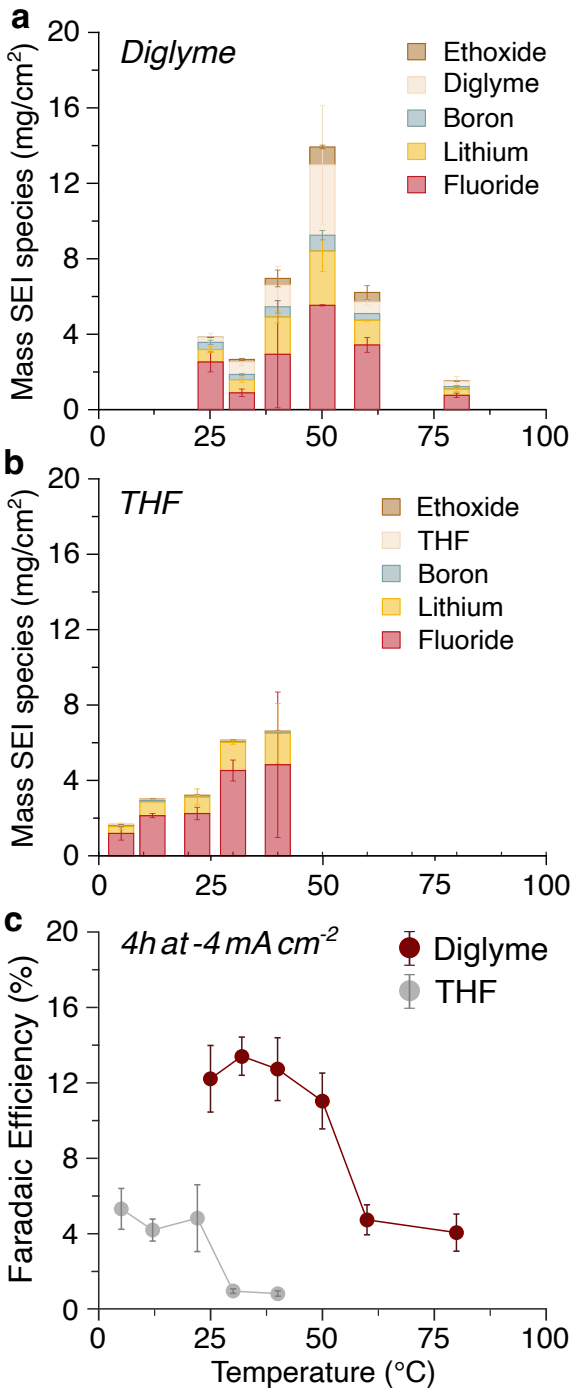

Figure 2. Composition of the SEI as a function of Li-N_2R temperature.

a-b) Mass of the species in the SEI rinsate as a function of temperature for the **a)** the diglyme and **b)** the THF electrolyte solvents. **c)** NH_3 Faradaic efficiency of the Li-N_2R reaction in diglyme and THF-based electrolytes as a function of temperature. For all experiments, a total charge of 16 mAh cm^{-2} was applied. Due to the low boiling point of THF (66 °C), Li-N_2R measurements could only be performed up to 40 °C for the THF-based electrolyte.

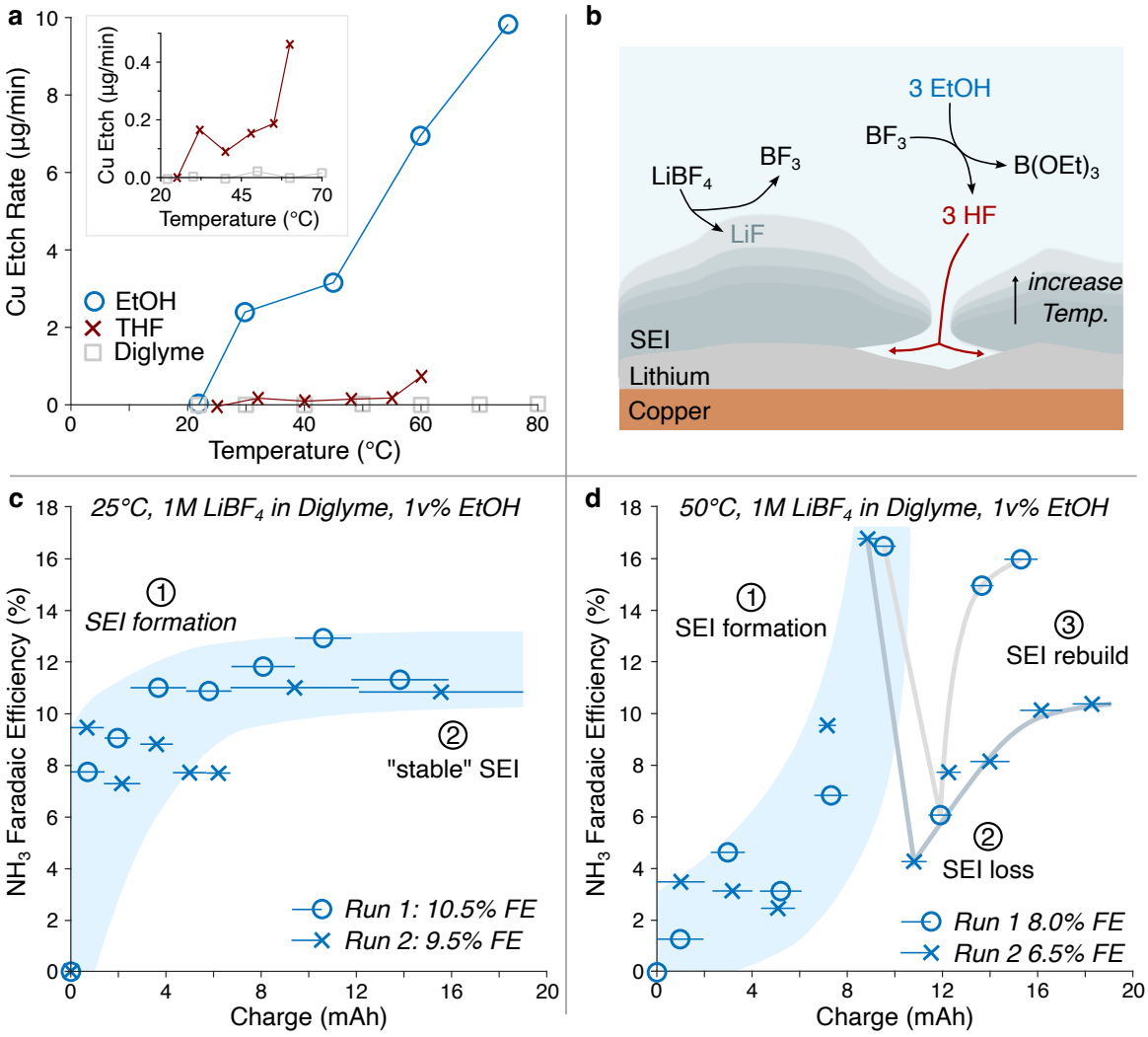

Figure 3. Temperature-dependent etching and its implications to Li-N_2R performance.

a) Cu etch rate as a function of temperature in solutions of 1M $LiBF_4$ in EtOH, 1 M $LiBF_4$ in THF, and 1M $LiBF_4$ in diglyme (see inset for detailed view on Cu etch rate in THF and diglyme). **b)** Proposed mechanism of the observed etching via the decomposition of $LiBF_4$ salts to form HF. **c-d)** Evolution of the NH_3 faradaic efficiency as a function of charge during Li-N_2R in 1M $LiBF_4$ in diglyme with 1% ethanol at a temperature of **c)** 25°C and **d)** 50°C. For each condition, two exemplary runs are shown. The Li-N_2R experiments were performed at constant current conditions with an applied current density of -4 mA cm^{-2}.

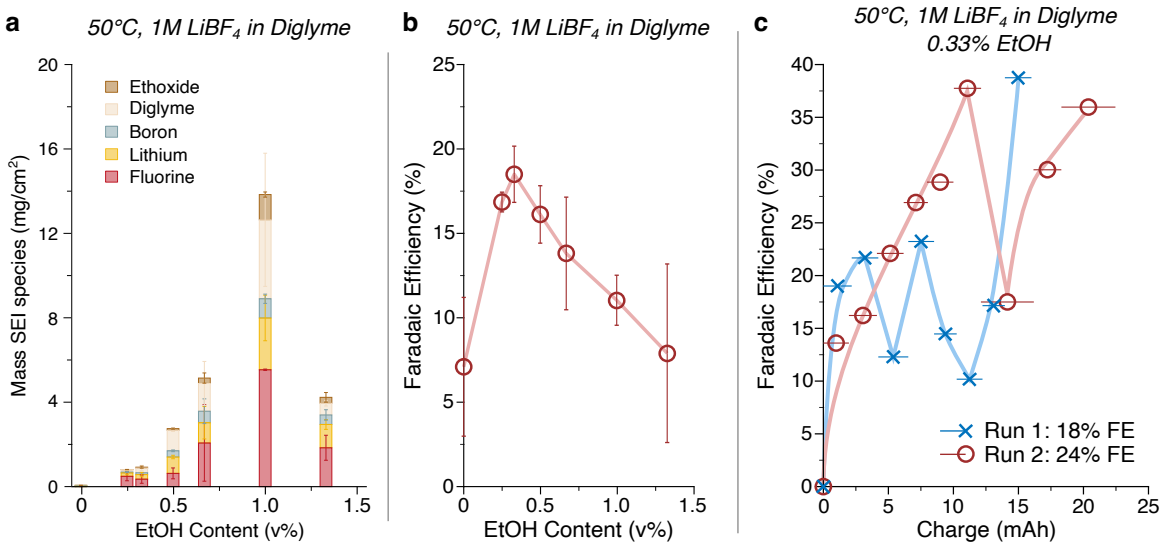

Figure 4. **Engineering the SEI at 50°C to increase Li-N_2R faradaic efficiency**

Study of Li-N_2R at 50°C as a function of EtOH content in the electrolyte, showing **a)** the chemical composition of the SEI as a function of EtOH content **b)** the evolution of the overall Faradaic efficiency (FE_{NH3}) after 16 mAh cm^{-2} of passed charge. **c)** Evolution of FE_{NH3} as a function of passed charge in a sample with 0.33v% EtOH. All experiments were performed at a constant current of -4 mA cm^{-2} in diglyme based electrolytes with 1M $LiBF_4$. For additional repetitions of this sampling run, see **Figure S10**.

Supplemental information

Document: Experimental Procedure, Figures S1 – S18, Tables S1-S7, Supplementary Note 1: Current cycling to elucidate SEI passivation properties

Table of content

I. Experimental Procedures

I.1. Materials

The following materials were used in this study: Copper (Cu, sheet metal 99.99%, 0.025" thickness, McMaster), Pt mesh (99.9% trace metal basis, 0.05cm thickness, Sigma), $LiFePO_4$ electrode sheet (LFP, single-sided coating on Aluminium, MTI Corp.), lithium tetrafluoroborate ($LiBF_4$, battery grade, Gotion), ultrapure water (18.2 MΩ, Millipore), ethanol (EtOH, anhydrous >99.5%. Sigma), diethylene glycol dimethyl ether (diglyme, anhydrous, 99.5%, Sigma), tetrahydrofuran (THF, anhydrous, >99.9%, inhibitor-free, Sigma), dimethyl sulfoxide-d_6 (d_6-DMSO, 99.9 at% D, Sigma), deuterium oxide (D_2O, 99.8% D ,TCI Chemicals), nitric acid (HNO_3, 70% >99.999% trace metal basis, Sigma), lithium standard for ICP (TraceCERT, 1 g/l in nitric acid, Sigma), boron standard for ICP (TraceCERT, 1 g/l in water, Sigma), fluoride standard for IC (TraceCERT, 1 g/l in water, Sigma), nitrogen (N_2, 99.999% ultra high purity grade, Praxair), argon (Ar, 99.999% ultra high purity grade, Praxair).

I.2. Electrochemical and Temperature-dependent Measurements

I.2.1 Electrochemical cell assembly

Unless stated differently, electrochemical experiments were run in single-compartment glass cells that contained four ports, allowing for the placement of three electrodes and a glass sparger that disperses the introduced gas (see **Figure S1a)**. For the working electrode (WE), a Cu electrode sheet was cut into a 3x1 cm strip, hand-polished with sandpaper, and subsequently rinsed with water and ethanol. The counter electrode (CE), a Pt mesh (height x width x thickness = 2.5 cm x 1 cm x 0.05 mm), was placed in the glass cell such that the Cu working electrode and the Pt mesh faced each other. For the reference electrode (RE), a $LiFePO_4/FePO_4$ electrode sheet was prepared via chemical delithiation of a commercial $LiFePO_4$ battery electrode sheet (see McShane et al.[1] for details).

The cell was assembled in a N_2-filled glovebox. First, the three electrodes were added to the glass cell, leaving only one port open. 15 ml of the electrolyte solution, typically a 1 M solution of $LiBF_4$ in THF or Diglyme with 1v% EtOH, was then introduced into the cell. Finally, the glass sparger, a custom-made glass piece (Adams and Chittenden Scientific Glass) that contains both a gas inlet line that disperses the gas through a frit and an outlet line that allows ensures that cell is not pressurized (see **Figure S1a**), is added to close the fourth port.

I.2.2 Temperature-dependent Li-N_2R experiments

Temperature-dependent Li-N_2R experiments over a temperature range of 2-80 °C were run in water baths. For this, the assembled cells were taken out of the glovebox into the preheated or precooled water bath and the inlet of the sparger was connected to a N_2 line (N_2 flow rate: approximately 20 ml min^{-1}) and a Biologic VMP-3 potentiostat. During the transfer, the sparger was open to air for less than 30 s. Water content measurements before and after transfer suggest that this approach did not lead to identifiable changes to the atmosphere (both were ~80 ppm water content).

After sparging the cell for 15 min, an electrochemical impedance spectroscopy run was performed to apply an ohmic resistance compensation. After resistance compensation, chronopotentiometry measurements were performed by applying either -1 mA cm^{-2} current between WE and CE for 2 h (2 mAh cm^{-2} charge) or -4 mA cm^{-2} current for 4 h (16 mAh cm^{-2} charge). Once the chronopotentiometry measurement was completed, the glass cell was sealed by removing the glass frit and rapidly closing the port with a lid. The glass cell was then transferred back into the glovebox where it was disassembled to retrieve the WE and the electrolyte for SEI and product characterization. The retrieved electrolyte volume was measured. For THF-based electrolytes the volume losses were due to evaporation were between 10 % at 5°C and 45 % at 40°C. For diglyme-based electrolytes, the losses due to evaporation

were nearly temperature independent at ~10%. As a result of the evaporation, the dynamics of the reaction might be affected and could lead to some differences between the THF and diglyme-based experiments. The trends across temperatures, however, should be unaffected. Other parts of the cell were then removed from the glovebox, washed with DI water and ethanol, and then stored in an oven at 80 °C.

For control runs in Ar, the same procedure was applied, only with the glass cell connected to an Ar line (Ar flow rate: approximately 20 ml min^{-1}).

I.2.3 Ammonia Faradaic efficiency (FE_{NH3}) sampling

To be able to measure the faradaic efficiency during a Li-N_2R run, 0.3 ml samples of the electrolyte were isolated to quantify the ammonia content. For this, the RE was replaced by a septum cap, resulting in a two-electrode setup with a Cu WE, a Pt mesh CE (**Figure S1b**). As for the temperature-dependent Li-N_2R runs described in experimental section 2.2, the cell was subsequently i) filled with electrolyte, ii) sealed in the N_2 glovebox, iii) transferred out of the N_2-filled glovebox into a preheated water bath, iv) sparged with N_2 for 15 min, v) the ohmic resistance of the electrolyte was determined via impedance spectroscopy, and iv) a chronopotentiometry experiment was performed at a current of -4 mA cm^{-2}. During the chronopotentiometry run, samples were taken out through the septum.

Note, that, as approximately 2% of the electrolyte was removed from the reaction for each aliquot, the current densities steadily increased, evidenced by a stepwise increase of the potential (see **Figure S2**). In addition, the potential fluctuated by approximately ~50 mV during the sample retrieval (see **Figure S2**). As a result, we anticipate that the observed overall reduction of the FE_{NH3} in comparison to the single batch reaction arises due to these disruptions

during the Li-N_2R.[2,3] The typical standard deviation of measured faradaic efficiencies was approximately within +/- 15%.

I.2.4 Conductivity measurements

Electrolyte conductivity measurements were performed in a single-compartment glass cell with the configuration shown in **Figure S1a**. During the measurement, the same electrolyte was heated stepwise from 2 °C to 60 °C. To equilibrate the electrolyte, the cell was kept 30 min at each temperature step before electrochemical impedance spectroscopy measurements were performed to quantify the resistance of the electrolyte.

I.2.5 Electrolyte Etching Studies

To study the amount of copper etched as a function of temperature, 1 M $LiBF_4$ was dissolved in either ethanol (dried over molecular sieves for 2 weeks, water content: < 60 ppm), THF, or diglyme (both water contents ~50ppm). In each run, a piece of copper (3x1 cm dimensions) was fully immersed into the electrolyte in a fully sealed glass cell. The cell was then heated stepwise to specific temperatures, where, after typically 1 hour, a 100 µL sample was taken. To quantify the Cu content in the electrolyte, 50 µL of that sample were then diluted to 10 ml with 0.1 M HNO_3. During the experiment, no electrodes were connected.

I.3. Quantification of Solid electrolyte interphase (SEI) species and Ammonia

I.3.1. Ammonia Quantification

Ammonia was quantified in electrolyte samples via a Bruker Neo 500 MHz nuclear magnetic resonance (NMR) spectrometer using a selective NH_4^+ pulsing technique.[4] For this, 500 µL of the electrolyte was acidified with 100 µL of a 0.5 M H_2SO_4 solution. Afterwards, 50 µL of ethanol and 500 µL of water were added to dilute the high concentration of electrolyte salt.

Finally, 25 µL of d_6-DMSO is added as a locking solvent. The obtained NMR spectra show a characteristic triplet. These peaks were integrated and compared to reference spectra (see **Figure S3**). Typical concentrations of ammonia after the experiment were between 50 µM and 1500 µM. Except for sampling experiments, both the NMR measurements of each run and the runs themselves were at minimum triplicated.

Once the concentration of the samples was obtained, the Faradaic Efficiency was calculated based on equation (1),

$$FE(\%) = \frac{3\ \alpha\ F\ [NH_3]_{NMR}\ V_{el}}{100 * Q},$$

where 3 is the amount of electrons required per NH_3 molecule, $[NH_3]_{NMR}$ is the concentration of NH_3 measured by NMR, Q is the charge passed during the experiment, V_{el} is the volume of the electrolyte after the reaction is completed, F is the Faraday constant, and α is a coefficient that accounts for the dilution of NH_3 in the NMR tube due to the introduction of the other species.

For sampling experiments, NMR sample preparation was prepared with half the volume of each reagent except d_6-DMSO (i.e., 250 µL sample, 50 µL H_2SO_4 solution, 25 µL EtOH, 25 µL d_6-DMSO, and 250 µL H_2O). Furthermore, to limit the size of the samples taken, these measurements could not be triplicated.

I.3.2. Preparation of SEI rinsates

To separate the SEI from the Cu electrode, the electrode was first gently washed with 2 mL of the electrolyte solvent. It was then dried in the N_2 glovebox for at least 24 h and transferred outside the glovebox in a sealed, septum-capped vial. 1 ml of D_2O was then introduced into the vial with a syringe, leading to a dissolution of most of the SEI species. After leaving the electrode sit in D_2O for at least 4 h, 600 µL of the rinsate solution was retrieved for further NMR characterization. Then, 200 µL and the Cu electrode sheet were added in 3.8 ml 0.1 M

HNO_3 where the Cu electrode was etched for at least a day, releasing all the remaining SEI species left on the electrode surface and allowing for further testing via ICP-MS and IC. For each condition (i.e., temperatures, EtOH contents, and electrolyte solvents), rinsates from at least three different experiments were used to measure the SEI composition.

I.3.3. Quantification of organic species: Nuclear magnetic resonance (NMR)

Diglyme, EtOH and THF contents within the SEI rinsates were quantified with a Bruker Neo 500 MHz nuclear magnetic resonance (NMR) spectrometer using a ^{1}H-NMR measurement. For this, integrated NMR peak intensities of the SEI rinsates were compared to a regression curve obtained from standard solutions in regions characteristic to each of the species to be studied (**Figure S4**).

I.3.4. Quantification of Li, B, and Cu: Inductively couple plasma mass spectrometry (ICP-MS)

ICP-MS measurements were performed with the Thermo Fisher iCAP RQ ICP-MS equipped with an autosampler. All species were quantified in STD mode using three sample runs and two washing steps after. To quantify Li and B in rinsate experiments, the SEI rinsate obtained after acid treatment was diluted between 50 to 1000 times in 0.1 M HNO_3. Then, three measurements were performed on different dilutions for each sample and compared to standards (see exemplary regression curves in **Figure S5**). For the Cu quantification after etching (see **Section 2.5**), 50 µL of the samples were diluted 200 and 1000 times in 0.1 M HNO_3. Note, that matrix property changes were observed due to the introduction of the electrolyte solvent into the ICP-MS. Therefore, 50 µL of the respective solvent were introduced to the 10 ml Cu standards.

I.3.5. Quantification of F: Ion chromatography (IC)

IC measurements were performed at the Stanford Environmental Measurements Facility on the Dionex ICS 6000. To quantify the fluoride content, the acidified SEI rinsate is diluted with water between 20 and 100 times, depending on the estimated concentration of the fluorides obtained through Li quantification at the ICP-MS (typical target concentration: 10 ppm).

I.3.6. X-ray photoemission spectroscopy measurements (XPS)

X-ray photoelectron spectroscopy (XPS) measurements were performed with a PHI VersaProbe 4 XPS using a monochromatic Al Kα X-ray excitation source ($h\nu$ = 1486.3 eV). The samples were transferred from the glovebox to the XPS chamber for analysis using a stainless-steel transfer vessel to avoid unwanted exposure to air. During measurements, a flood gun with low-energy electrons and argon ions was used to offset sample charging. The survey spectra were recorded with a step size of 1.0 eV and a dwell time of 20 ms at a pass energy of 224 eV. High-resolution scans were collected with a step size of 0.1 eV and a dwell time of 20 ms at a pass energy of 55 eV. To understand the chemical composition through the SEI layers, depth-profiling measurements were recorded with an ion gun at 4 kV and 3 μA mode with a scanning size of 2×2 mm2 for five core levels (Li 1s, B 1s, C 1s, O 1s, and F 1s) at three different sputter times (0 min, 2 min, and 10 min). All core-level spectra were energy-referenced to the LiF peak at 684.8 eV. The IGOR Pro software was used for data analysis where Voigt functions were employed to deconvolute the peaks after subtracting a Shirley background function.

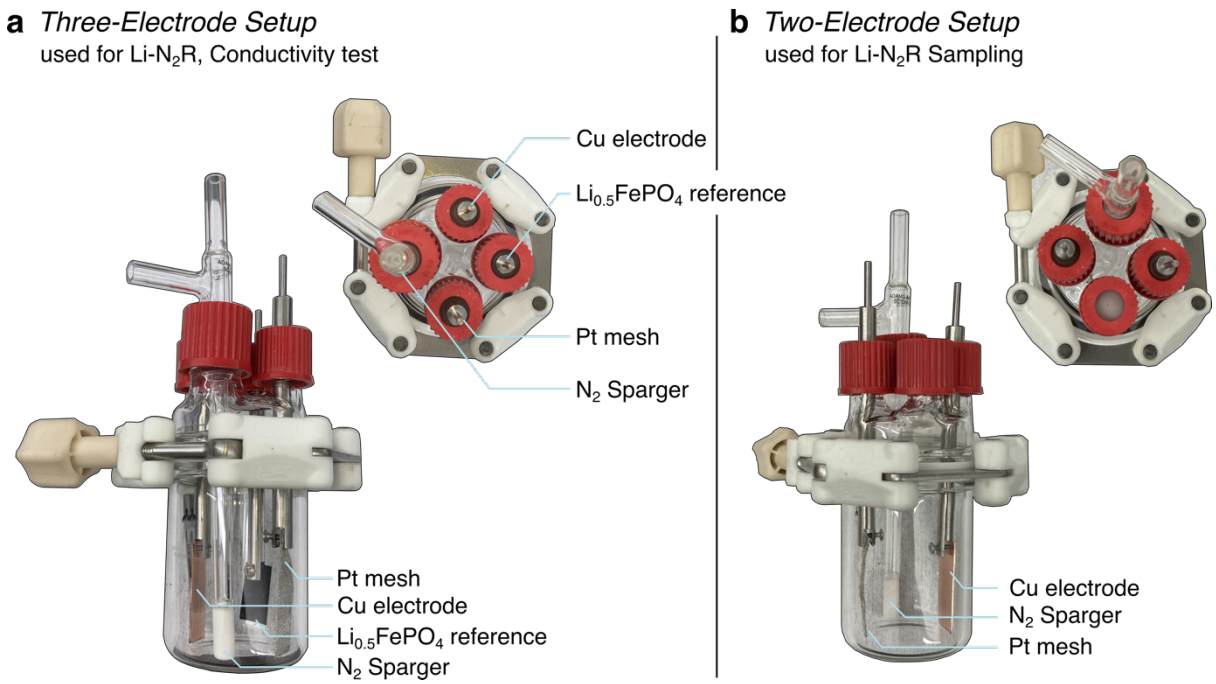

Figure S1. Images of the glass cell in **a)** three-electrode and **b)** two-electrode configuration.

For clarity, side views and top views of the cell are provided.

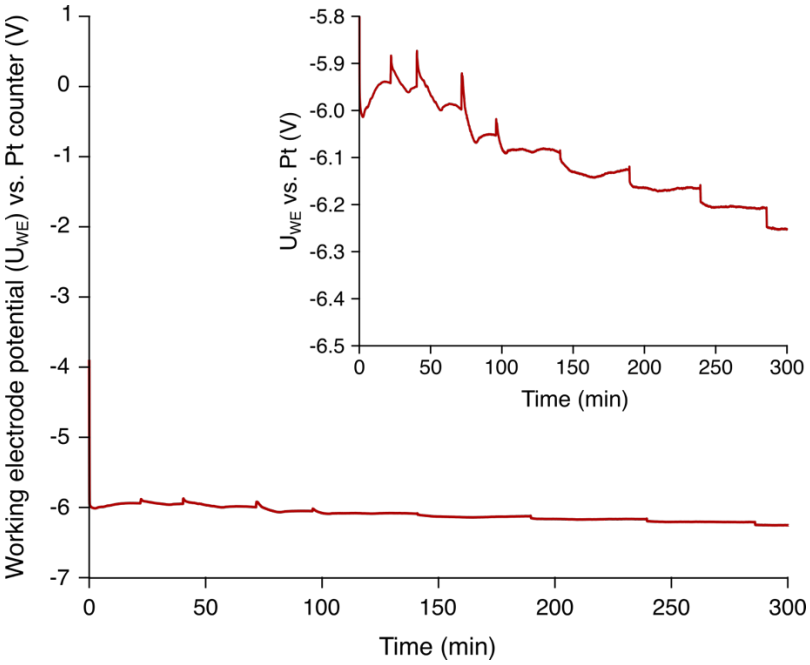

Figure S2. Potential of the Cu working electrode during a Li-N_2R sampling run in a two-electrode setup. With every sample taken, we observed a first pike of potential due to the introduction of the syringe into the cell, followed by a dip of the potential as the electrolyte volume is reduced by 300 µL (see inset). Overall, however, the potential changes are minor.

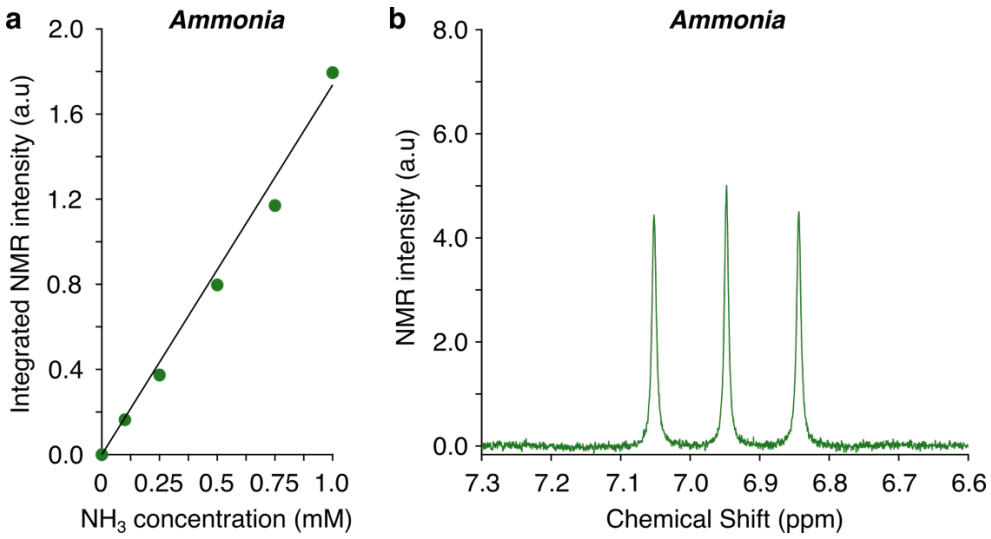

Figure S3. **a)** Integrated intensity of ammonia references obtained via ^{1}H NMR by integrating the characteristic $^{14}NH_4^+$ triplet peak (shown in panel **b)**.

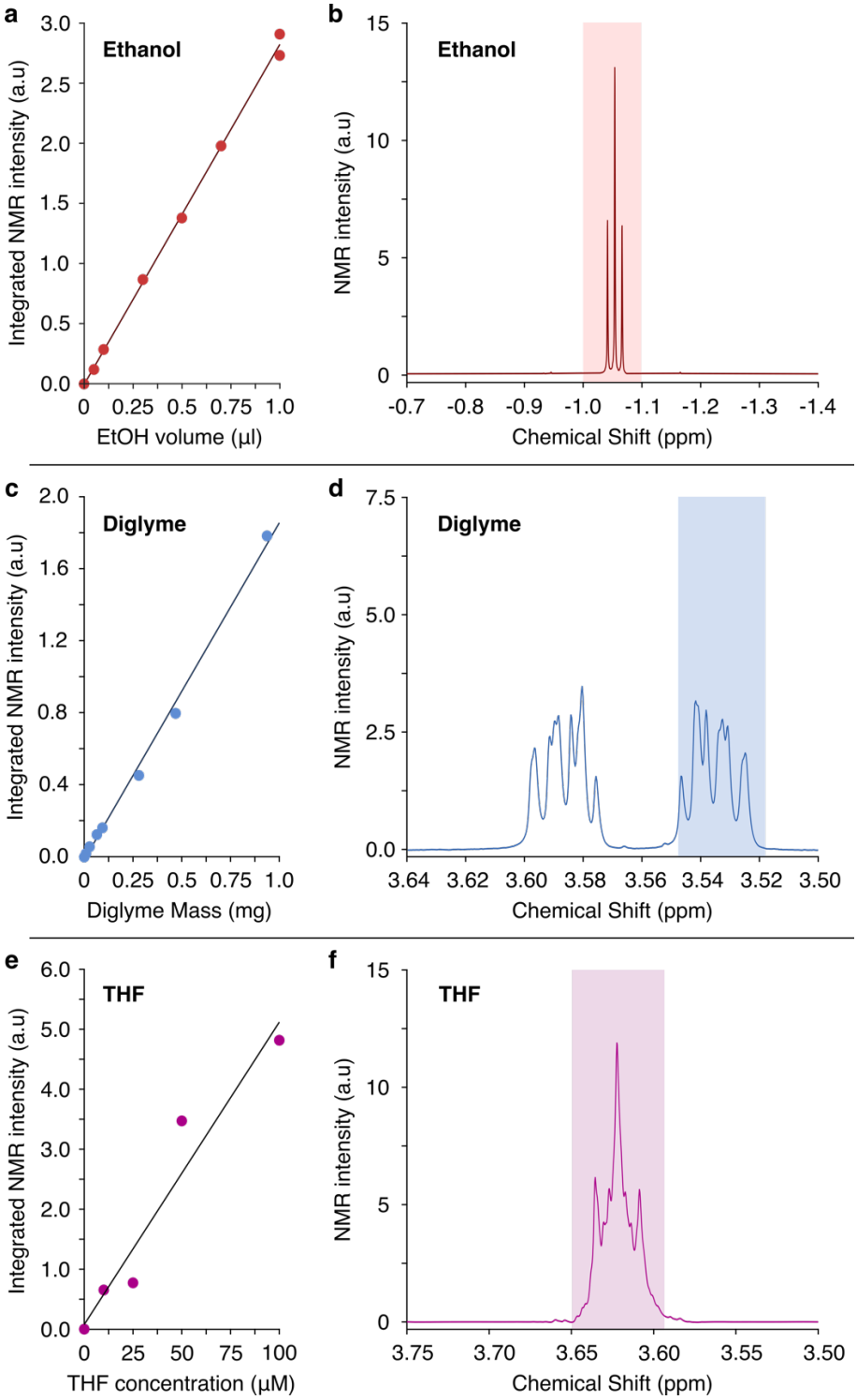

Figure S4. *Linear regression of the integrated ^{1}H-NMR peak intensity of standards containing* ***a-b)*** *EtOH,* ***c-d)*** *diglyme,* ***e-f)*** *THF. Each standard consists of 600 µL of the dissolved organic species in D_2O (organic content between 0 to 1 µL) and 25 µL of d_6-DMSO. Peak integrations were performed on characteristic peaks. The regions for integration are specified in panel* ***b)*** *for EtOH,* ***d)*** *for diglyme and* ***f)*** *THF, respectively.*

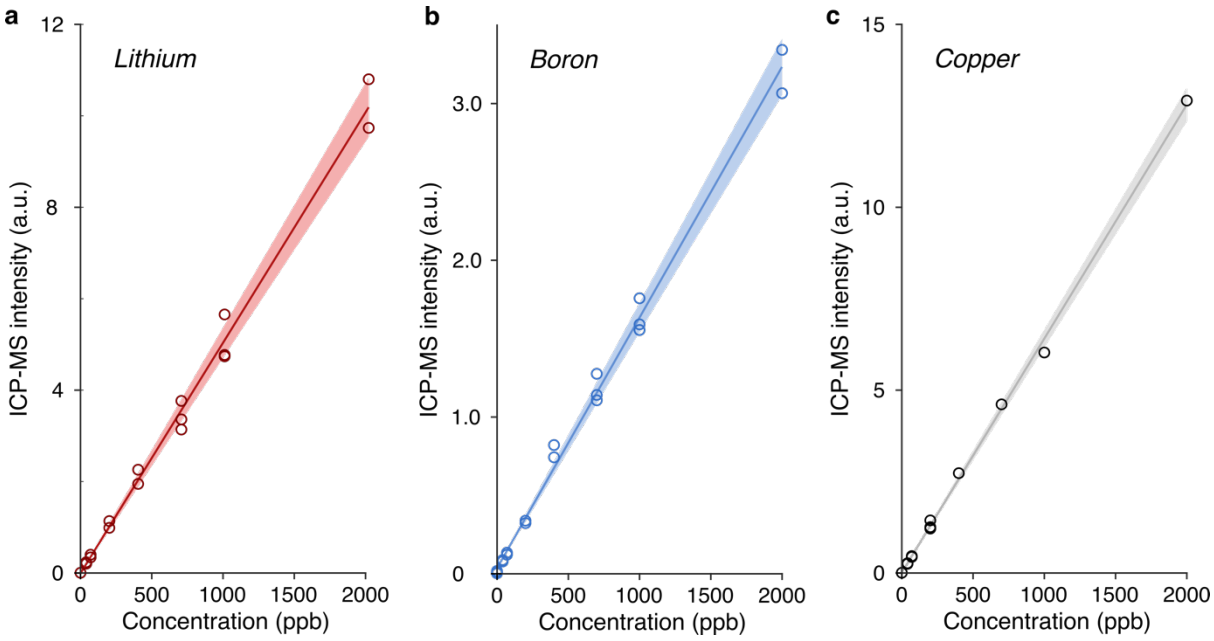

Figure S5. Exemplary ICP-MS standard measurements for **a)** lithium, **b)** boron, and **c)** copper. To account for daily variations of the ICP-MS, the standard measurements are performed on the day of measurement. To assure the stability of the ICP-MS during the measurement, additional standard points are measured between samples.

II. Supporting Results

Figure S6. Temperature dependence of Li-N_2R at early reaction stages

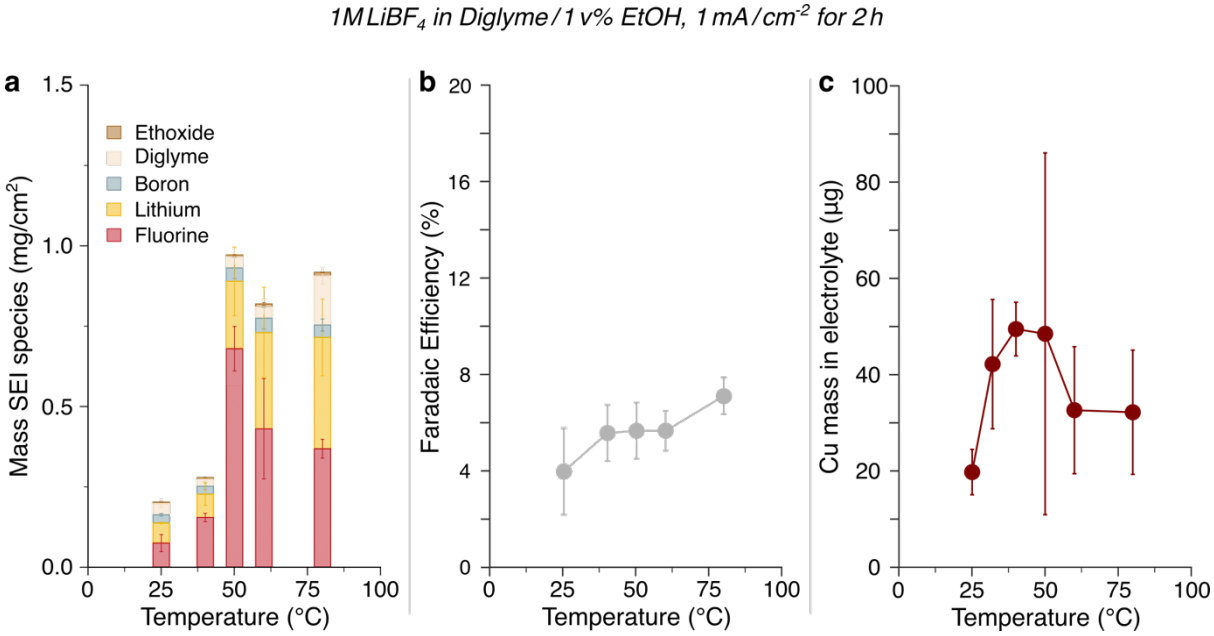

Figure S6. a) Composition of the SEI as a function of temperature after 2 mAh cm^{-2} of charge is passed in diglyme-based electrolytes. Initially, the composition rises with temperature until it becomes approximately constant above 50 °C. **b)** Evolution of NH_3 Faradaic efficiency (FE_{NH3}) as a function of temperature after 2 mAh cm^{-2} of charge is passed. We observe an overall increase of with increasing temperature. **c)** Mass of Cu etched during Li-N_2R as a function temperature after 2 mAh cm^{-2} of charge is passed. We first see an increase of the etched Cu up to 40 °C. Above 40 °C, the amount of etched Cu is dropping. Together with the unexpected plateauing of the SEI species observed at those temperatures, we hypothesize that the HF generated at higher temperatures primarily etches the SEI.

Figure S7. Characteristic Electrochemical Potentials of 16mAh experiments

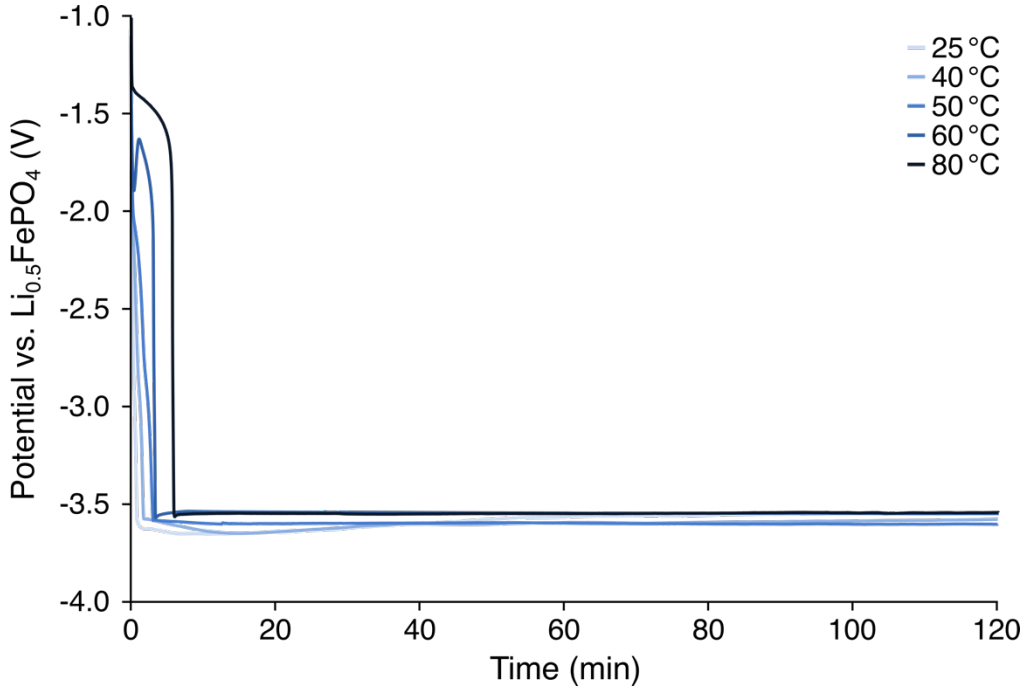

Figure S7. Electrochemical potential of the Li-N_2R working electrode versus a $Li_{0.5}FePO_4$ reference, V_{LFP}. In these experiments, a constant current of -4 $mAcm^{-2}$ is applied at different temperatures. All experiments lead to approximately the same plateau potential of -3.5V vs. V_{LFP}, characteristic for the potential of lithium deposition. As the temperature is increased, the time to reach the lithium electrodeposition potential is increased, which suggests an increased SEI formation rate at higher temperatures.

Figure S8. Images of the SEI with THF-based electrolytes

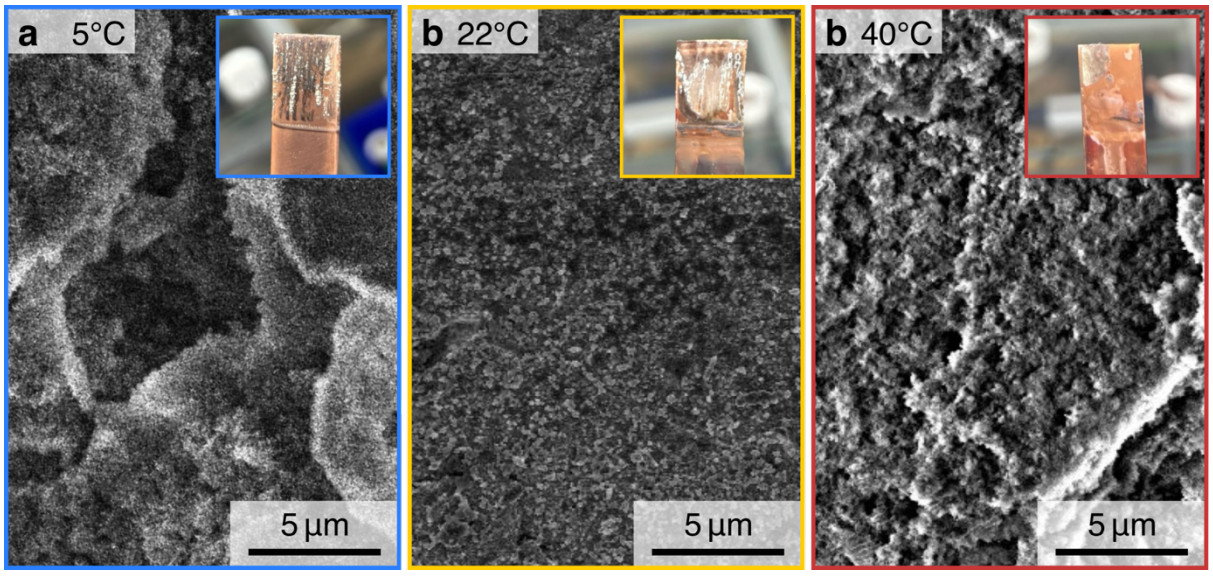

Figure S8. Scanning electron microscopy (SEM) images and photographs of the SEI obtained from THF-based electrolytes at **a)** 5 °C, **b)** 22 °C, and **c)** 40 °C. At 5 °C, we observe a strongly irregular and porous SEI. At 22 °C, a regular thin film forms. That film becomes significantly thicker at 40 °C, as evidenced by the charging observed during SEM imaging. We also observe a loss of SEI on the Cu surface, suggesting etching of the SEI.

Figure S9. SEM images of the SEI with Diglyme-based electrolyte

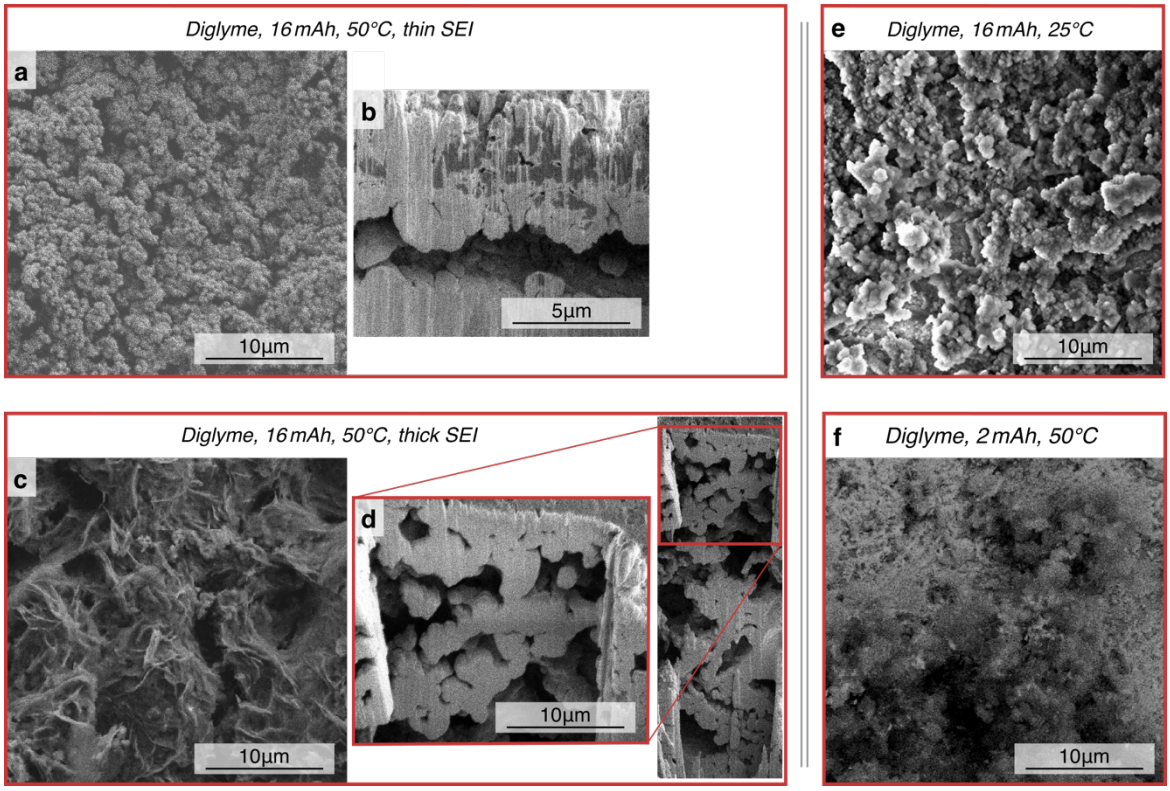

Figure S9. Scanning electron microscopy (SEM) images of the SEI obtained in diglyme-based electrolytes under different conditions. **a-d)** SEM images obtained after a Li-N_2R run at 50 °C with a passed charge of 16 mAh cm^{-2}. We observe areas thinner areas that develop a thick, highly porous inorganic-rich SEI (**a,b**) and of organics-rich, thick SEIs (**c,d**). Focused ion beam (FIB) cross sections reveal a highly porous network within the SEI layer that can even form cavities. **e)** SEM image obtained after a Li-N_2R run at 25 °C with a passed charge of 16 mAh cm^{-2}. **f)** SEM image obtained after a Li-N_2R run at 50 °C with a passed charge of 2 mAh cm^{-2}.

Supplementary Note 1. Current cycling to elucidate SEI passivation properties

One of the key ways how the SEI dictates Li-N_2R performance is by influencing the mass transport properties of key chemical species at the electrode interface. Given the thickness of the SEI and the nature of the reaction with multiple reactive species involved, it is attractive to study mass transport via a bottom-up approach, where measurements of the microstructure and composition via methods such as (cryo-)electron microscopy and x-ray scattering lead to a model for species transport. Unfortunately, the SEI is a highly complex interfacial layer that is i) electronically insulating, ii) composed of both crystalline and amorphous species, iii) made up from light elements, and iv) dynamically changing during the reaction. Consequently, it would be extremely difficult to perform a bottom-up approach to study mass transport in the SEI in a manner that would fully capture these complexities.

Instead, we considered a top-down approach where we used the rate of lithium metal oxidation, r_{Li}, during Li-N_2R as a proxy for mass transport and microstructural differences between different SEIs. We motivate this approach by imagining two opposite situations (**Figure S10**). First, if a layer of Li is located under a perfectly passivated SEI, similar to ones obtained in Li metal batteries (**Figure S10a**), the mass transport of Li metal and other reactive species (e.g., N_2, protons, electrolyte) is zero and and $r_{Li} = 0$. In contrast, when there is no SEI present, e.g., at the beginning of the Li-N_2R reaction, r_{Li} will be maximal (**Figure S10b**). In scenarios between those two extrema (**Figure S10c**), we hypothesize that r_{Li} will be somewhere in between and depend on the complex interaction of mass transport rates of reactive species, which in turn depends on the microstructure and composition of the SEI.

$$r_{Li} = \frac{dn_{Li}}{dt} = f(r_H, r_{N_2}, r_{el}, \dots)$$

Assuming that r_{Li} is time-independent, the rate can then be written as a function of the total amount of lithium metal, $n_{Li,tot}$ and the the time until Li is fully depleted, t_{Li}.

$$n_{Li,tot} = \int_0^{t_{Li}} r_{Li}\, dt = t_{Li} r_{Li}, \qquad if \left(\frac{\partial r_{Li}}{\partial t}\right) = 0$$

As a result, not only r_{Li} but also t_{Li}, which can be readily measured using electroanalytical techniques, becomes a qualitative marker for the passivation of the Li surface during Li-N_2R when the amount of deposited lithium is known.

We determined t_{Li} by applying a current cycling approach (**Figure 10d-f**). We first electroplated lithium metal at a current of -4 mA/cm^2 for 2 min, corresponding to approximately 65 µm of deposited Li (**Figure S10d**). We then set the current to zero and let the system relax under open circuit conditions (**Figure S10e**). Thereby, the potential settled first at the Li/Li$^+$ reduction potential (~-3.4 V vs. LFP), suggesting the presence of unreacted Li. Once all Li is consumed or electrically disconnected from the electrode (**Figure S10f**), the cathode potential becomes substantially less negative and, once the cutoff potential of -2.8 V vs. LFP is reached, a new electroplating cycle was started. The overall time at open circuit correlates directly with t_{Li}, thus allowing us to compare the passivation of the SEI at a given amount of passed charge. We therefore do not only obtain ex situ SEI characterization but continuously monitor the passivation of the SEI as a function of passed charge, which, to the best of our knowledge has not been shown for Li-N_2R before.

Note that the electrode potential can also become less negative than the Li/Li$^+$ potential when the Li metal is electrically disconnected from the electrode. Such dead lithium is often found in Li metal batteries during fast lithium stripping[5]. However, as the electrolyte itself is

chemically depleting the lithium metal and no stripping current is needed, the amount of unreacted, electrically disconnected lithium is expected to be negligible.

In the following, we provide two situations that give important supporting information for the claims made in the main text of this publication. First, we will validate the technique and confirm the appearance of SEI fluctuations by studying how the proton source affects passivation and SEI formation dynamics at 50 °C. Second, we will compare the passivation of the Li surface as a function of electrolyte solvent, confirming that the THF electrolyte leads to a more passivating SEI at elevated temperatures.

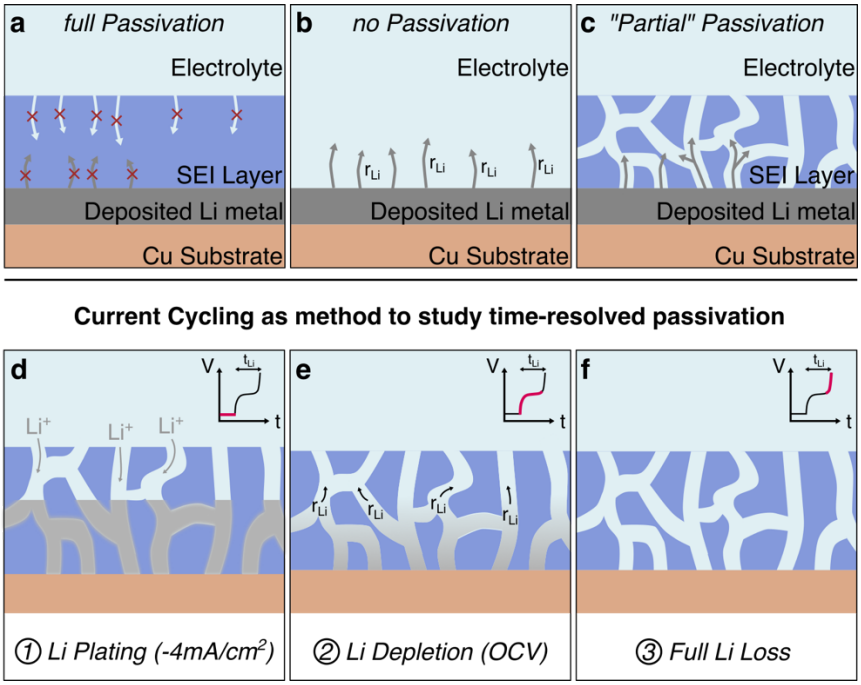

Figure S10. a-c) Schematic depiction of different hypothetical passivation conditions and their effect on lithium decomposition. **a)** Full passivation by the SEI, where both electrolyte and lithium cannot traverse through the SEI. **b)** No passivation, where the rate of Li decomposition is maximized. **c)** A hybrid scenario with a porous SEI, where the electrode partially passivated. **d-f)** Proposed current cycling approach to measure the Li decomposition time, t_{Li}, during Li-

N_2R. First, a constant layer of Li is deposited (**d**), that Li layer is left to decompose during OCV conditions (**e**) until all lithium is reacted away and a new cycle is started (**f**). Inset: expected behavior of the electrochemical potential during each of the steps.

The role of proton-source in SEI passivation

To validate whether this approach led to meaningful information about SEI passivation, we applied the current cycling approach to Li-N_2R at 50 °C in a 1 M $LiBF_4$ solution in diglyme with or without 1%v EtOH (**Figure S11**). Consistent with previous studies[6], we observed that t_{Li} is initially strongly increased to more than 10 min without the presence of a proton source. Over time, the diglyme oxidation at the anode generates protons that end up dissolving the passivated SEI and decrease t_{Li}, supporting our findings of nonzero FE to NH_3 upon extensive cycling (see **Figure 4**).

The evolution of t_{Li} with EtOH present was also qualitatively consistent with our model. As protons will readily react with lithium to form H_2 and NH_3, t_{Li} is initially less than 5 seconds. With progressing formation of the SEI as total charge passed increases, t_{Li} slowly increases to the range of ~100 s after 15 mAh of charge is passed, further supporting the idea that maximal passivation is achieved only when Li-N_2R is run for a sufficiently long period. Interestingly, fluctuations in t_{Li} are observed beyond 15 mAh of charge passed, which we hypothesize could be due to the loss of SEI observed earlier (see **Figure 3**).

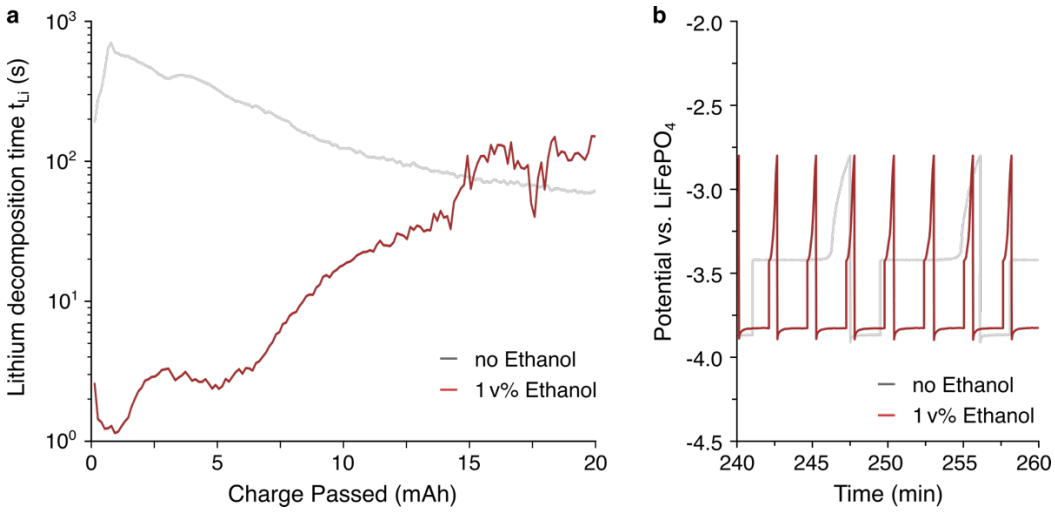

Figure S11. **a**) Lithium decomposition time, t_{Li}, as a function of passed charge during Li-N_2R. The reaction was performed at 50 °C in a diglyme-based solution containing 1 M $LiBF_4$ and either 1v% EtOH (red) or no Ethanol (dark grey). Note the semilogarithmic scale in t_{Li} and the two orders of magnitude longer lithium decomposition time without EtOH present. **b**) Voltage profile of the two different experiments after 240 min. Without Ethanol present, a plateau is found at the Li/Li^+ potential. With Ethanol, however, only a small shoulder is visible.

The role of the electrolyte solvent in SEI passivation

Our findings regarding the composition of the SEI via rinsate analysis (see **Figure 2**) and XPS (see **Figure S13**) suggest that THF-based electrolytes incorporate significantly less organic species in the SEI compared to the diglyme-based electrolytes. We hypothesized that the decrease in organic species lead to a more passivating and brittle SEI with THF as electrolyte solvent, leading to a reduction of species transport, SEI loss and overall performance loss once the SEI mass becomes large at elevated temperatures. To validate this hypothesis, we applied the current-cycling approach to measure t_{Li} while running Li-N_2R with either diglyme or THF-based electrolytes. We chose a reaction temperature of 30 °C which allowed for the study of enhanced SEI growth with less than 40% THF loss (by volume) due to evaporation. We observed significant differences in passivation behavior between THF and diglyme-based

electrolytes (**Figure S12a)**. In the diglyme-based electrolyte at 30 °C, t_{Li} is initially very small (< 5 s) and then steadily increases throughout the measurement up to close to 20 s after 16 mAh/cm^2 of charge passed. This behavior follows the trend observed with the diglyme-based electrolyte at 50 °C (see **Figure S11**). However, t_{Li} is much smaller in magnitude after 16 mAh/cm^2 charge is passed at 30 °C. Furthermore, while t_{Li} leveled off in the 50 °C experiment after 15mAh/cm^2 of charge passed, t_{Li} is steadily increasing at 30 °C. Together with the smaller amount of SEI deposited at the lower temperature (see **Figure 2**), this indicates that the SEI might not be fully formed, yet. Interestingly, no fluctuations are observed at 30 °C, supporting the hypothesis that etching and SEI loss occur mainly at higher temperatures.

In the THF-based electrolyte, t_{Li} increases first to 45 s at 2 mAh/cm^2, after which it drops and then varies between 15-40 s. This result is in strong contrast to the diglyme-based electrolyte and suggests a stronger passivation at earlier times. In addition, the variation of the passivation suggests some instabilities in the SEI e.g., due to cracking or delamination. If such a behavior happens, it was shown by Deissler et al.[6] that mainly LiH forms, leading to a very low FE. The idea of cracking is further supported by the composition of the THF-based SEI, that is very poor on organic species and hence very brittle (see **Figure 2** and **Figure S11a**).

While the current cycling approach shown here gives qualitative insights into the passivation of Li and hence allows to study properties of different SEIs that, to the best of our knowledge, have not yet been accessible, we note that there are three important limitations to this approach. Firstly, t_{Li} does not only depend on the degree of passivation but also on thermodynamic (e.g., temperature, pressure) and kinetic parameters that affect Li reactivity. It also cannot reveal microscopic differences of the SEI. Thirdly, drawing direct conclusions from t_{Li} to FE is too simple as passivation and Li reactivity are not guaranteeing perfectly matched Li^+, N_2 and H^+ mass transport rates. Nonetheless, this technique, in concert with the rinsate, XPS, and FE study

presented here, provided new insights and thus shows promise to become a regularly applied tool for Li-N_2R characterization.

Finally, we note that, by reducing the current cycling approach to the single parameter t_{Li}, a lot of interesting additional data is lost, as shown by the different potential profiles shown **Figures S12b** and **S12c**. While analyzing these differences of potentials could potentially lead to rich scientific findings, they are beyond the scope of this study.

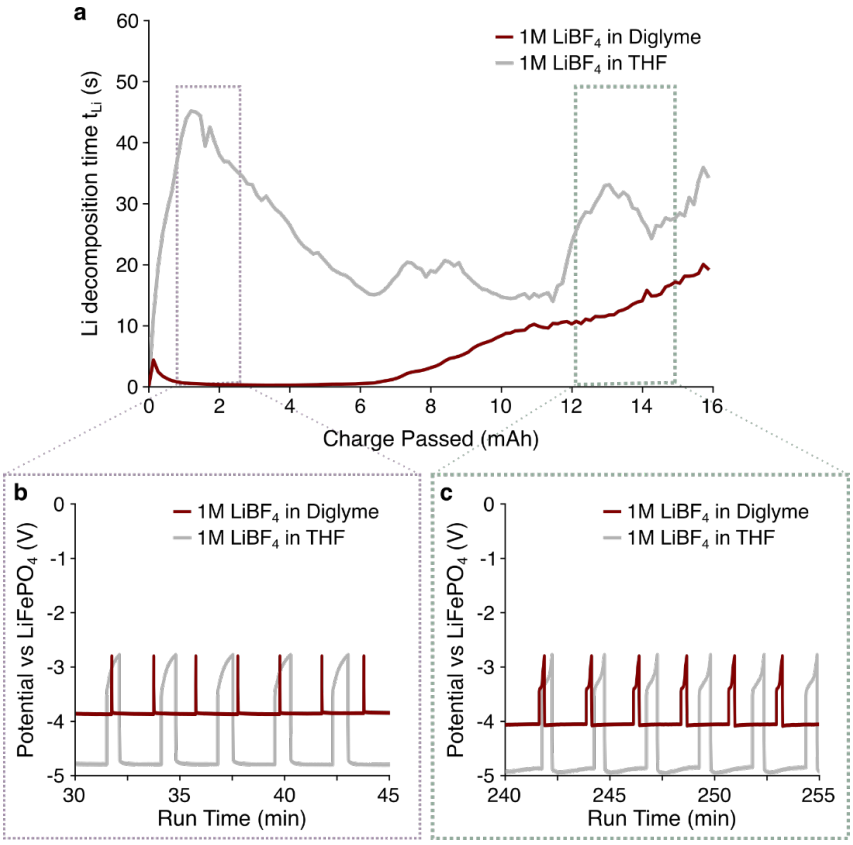

Figure S12. a) Li decomposition time t_{Li} obtained from current-cycling experiments during Li-N_2R, as a function of charge passed for THF-based (grey) and Diglyme-based electrolytes (red). In both cases, Li-N_2R measurements were performed at 30 °C with the electrolyte solution containing 1 M $LiBF_4$ and 1 v% EtOH. **b-c)** Potential profile of the current-cycling experiments as a function of time for early (**b**) and late cycles (**c**), marked with their approximate position in **a)**.

Figure S13. Depth-resolved XPS of SEIs: Diglyme-based electrolytes

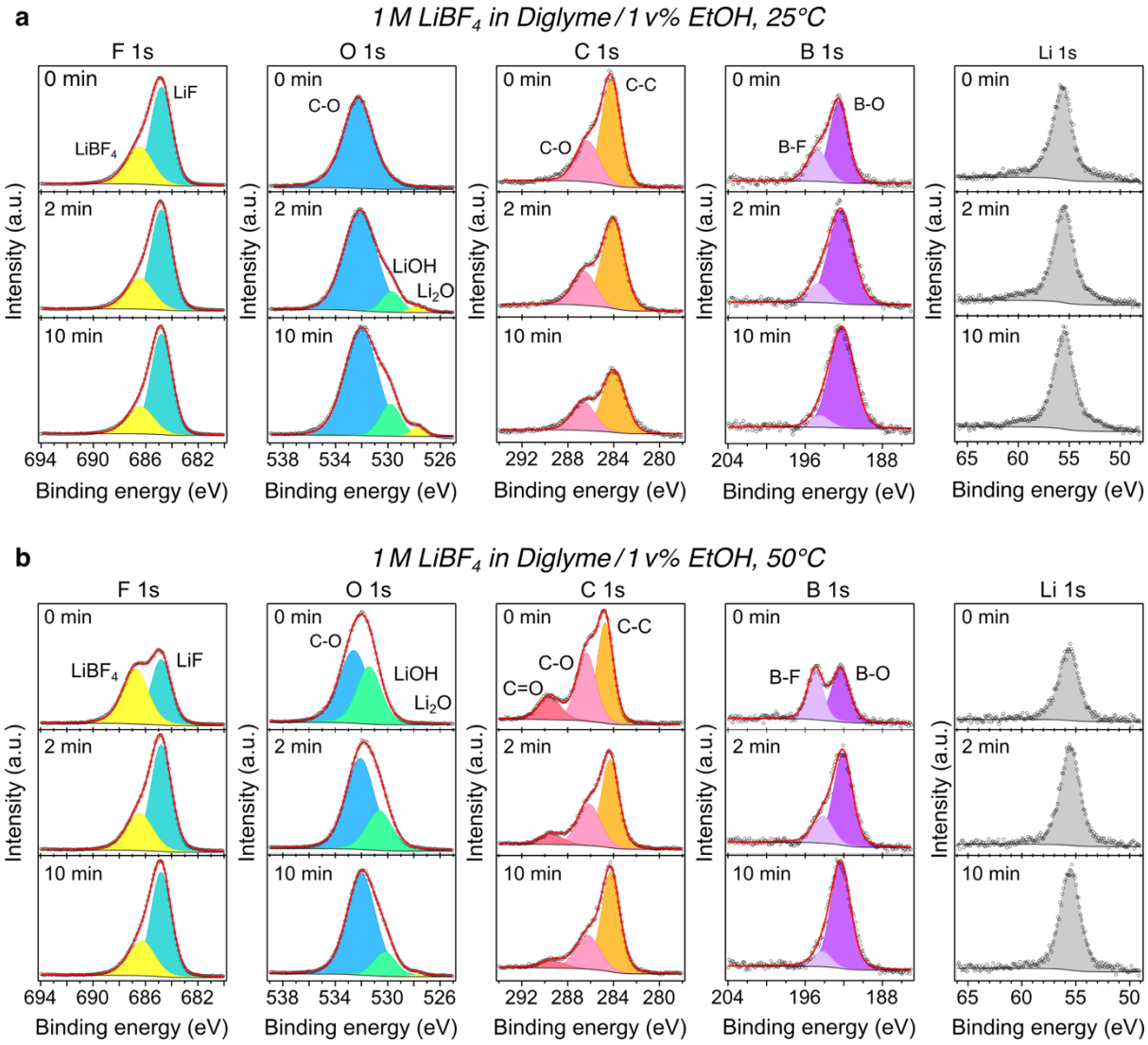

Figure S13. Ex situ measurement XPS spectra of SEIs made from diglyme based electrolytes, containing 1 M $LiBF_4$ in diglyme / 1v% EtOH, after 16 mAh/cm^2 of charge passed. For depth-resolution, samples were compared at a sputtering time of 0, 2, and 10 min. **a**) SEI after Li-N_2R experiment at 25°C. With increasing sputtering, we observe the reduction of B-F, $LiBF_4$, and C-C species, while LiOH, and LiO_2 increase. **b**) For Li-N_2R at 50 °C, we observe the same trends. We also find some bonds in the energy range characteristic for C=O bonds that seen to reduce at higher energies. All samples, show the occurrence of B-O bonds indicative of a borate species and BF_4 decomposition. For typical energies of relevant species, see **Table S2.**

Figure S14. Depth-resolved XPS measurements of SEIs from THF-based electrolytes

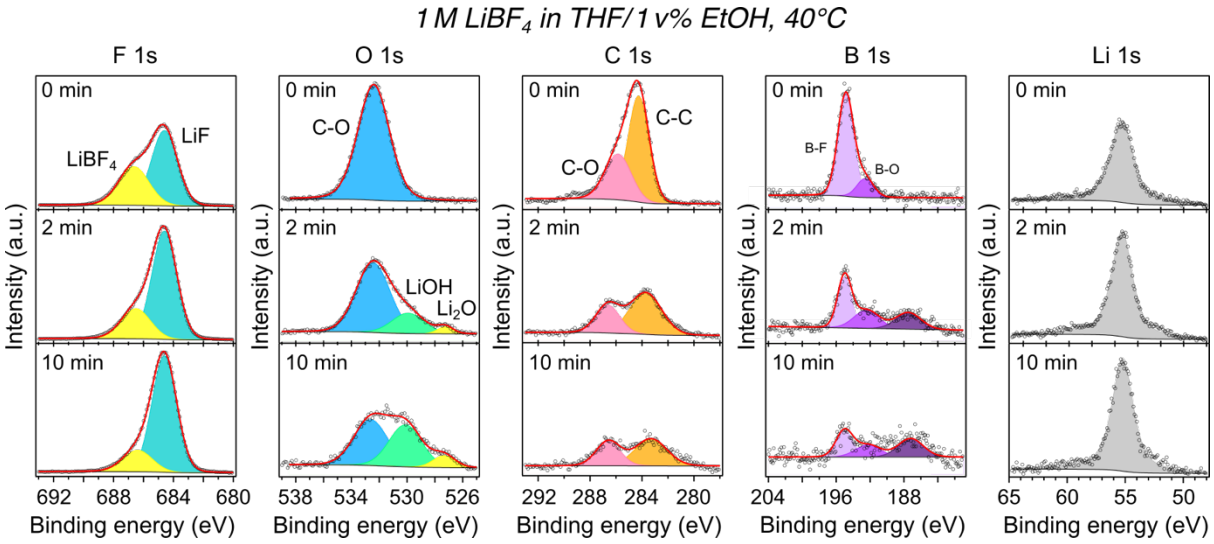

Figure S14. Ex situ measurement XPS spectrum of the SEI made electrolytes at 40 °C from THF-based, containing 1 M $LiBF_4$ in THF / 1v% EtOH, after 16 mAh/cm^2 of charge passed. For depth-resolution, samples were compared at a sputtering time of 0, 2, and 10 min. With increasing sputtering, we observe a strong decrease of the C-O and C-C bonds, suggesting that Carbon is mainly located at the particles surface and less so deep within the SEI. We also observe an additional species in the B 1s energy range. Given the energy range that is close to B-C bonds (see **Table S3**), we hypothesize that this peak could arise from a THF-BF_x complex that is known to occur.[7]

Figure S15. XPS Survey spectra of SEIs

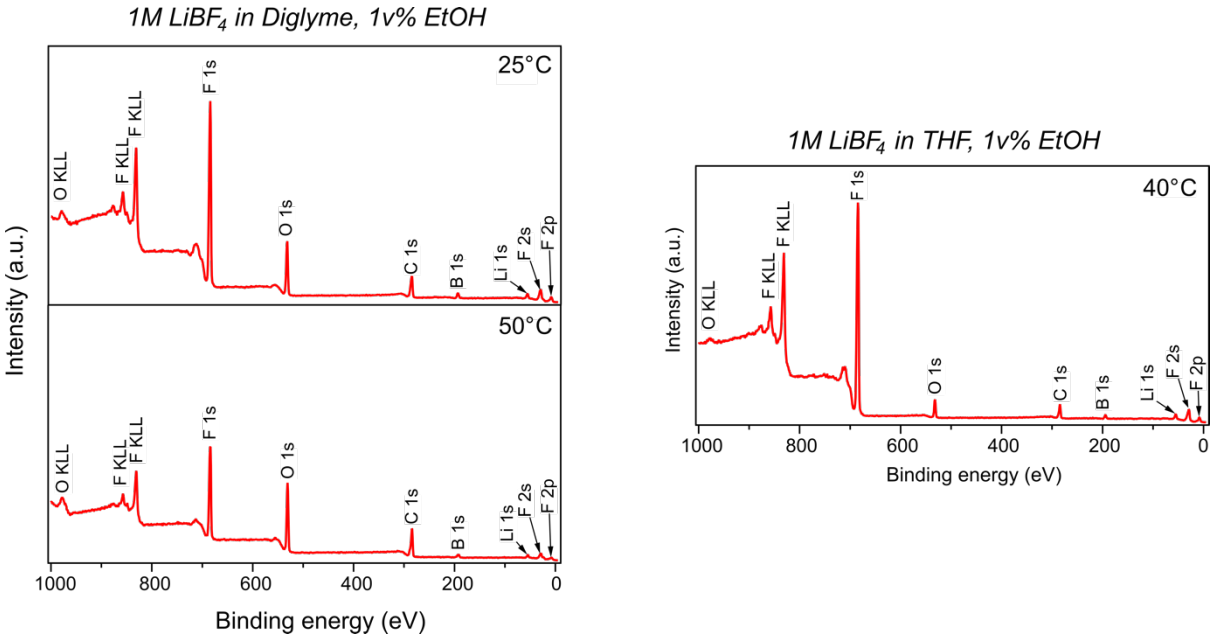

Figure S15. XPS survey spectra of the SEI shown in Figure S12 and S13 at 0 min etch time. Only, F, O, C, B, and Li are observed. In addition, the amount of C species in the THF-based electrolyte as strongly reduced in comparison to the diglyme-based electrolyte, while the F species are larger in amount, indicative of a more inorganic SEI.

Table S1-S5: Fitted Values of Depth-resolved XPS experiments

Table S1. Fit Values used to fit detailed XPS spectra in the region of the F 1s edge. The parameters represent: ai, area of peak i; pi, position of peak i; wi, FWHM of peak i.

	F 1s									
	Diglyme 25 °C			Diglyme 50 °C			THF 40 °C			
	0 min	2 min	10 min	0 min	2 min	10 min	0 min	2 min	4 min	10 min
a1	9.41E4	9.65E4	9.61E4	4.04E4	6.65E4	6.42E4	8.93E4	1.23E5	1.25E5	1.31E5
p1	684.1	684.0	683.9	683.6	683.7	683.7	684.2	684.2	684.2	684.1
w1	1.91	1.92	1.90	1.82	1.84	1.83	2.04	1.95	1.94	1.94
a2	4.49E4	3.75E4	3.27E4	4.31E4	2.92E4	2.72E4	5.38E4	4.01E4	3.48E4	2.87E4
p2	685.8	685.7	685.5	685.6	685.3	685.2	686.2	686.1	686.0	685.9
w2	2.42	2.42	2.40	2.32	2.34	2.33	2.39	2.30	2.29	2.29

Table S2. Fit Values used to fit detailed XPS spectra in the region of the B 1s edge. The parameters represent: ai, area of peak i; pi, position of peak i; wi, FWHM of peak i.

	B 1s									
	Diglyme 25 °C			Diglyme 50 °C			THF 40 °C			
	0 min	2 min	10 min	0 min	2 min	10 min	0 min	2 min	4 min	10 min
a1	2418	3673	3936	1746	3130	3761	354.3	508.8	473.8	393.3
p1	191.8	191.5	191.3	191.1	191.0	191.3	192.2	192.1	191.9	190.1
w1	2.3	3.0	3.0	2.224	2.3	2.4	2.4	3.5	3.5	3.0
a2	994.7	597.7	374.3	1403	938.8	491.6	1810	788.1	701.3	522.0
p2	194.1	193.9	193.6	193.7	193.1	193.2	194.5	194.7	194.5	194.4
w2	2.412	2.412	2.412	1.89	2.35	2.155	2.203	1.939	2.05	2.35
a3	-	-	-	-	-	-	-	462.6	415.6	568.5
p3	-	-	-	-	-	-	-	187.1	187.2	186.2
w3	-	-	-	-	-	-	-	3.5	3.5	3

Table S3. Fit Values used to fit detailed XPS spectra in the region of the C 1s edge. The parameters represent: ai, area of peak i; pi, position of peak i; wi, FWHM of peak i.

	C 1s									
	Diglyme 25 °C			Diglyme 50 °C			THF 40 °C			
	0 min	2 min	10 min	0 min	2 min	10 min	0 min	2 min	4 min	10 min
a1	8600	8378	5949	9751	9308	1.097E4	5444	3269	2983	2127
p1	283.5	283.3	283.1	283.5	283.2	283.2	283.8	283.3	283.1	282.8
w1	1.990	2.285	2.350	1.658	1.805	1.881	1.894	2.897	2.897	2.897
a2	4030	3299	2768	7832	5590	4723	2969	1657	1593	1468
p2	285.6	285.8	285.8	285.1	285.1	285.2	285.4	286.3	286.2	286.1
w2	2.390	2.350	2.350	1.958	2.305	2.381	2.394	2.186	2.155	2.200
a3	-	-	-	2934	1312	1012	-	-	-	-
p3	-	-	-	288.3	288.3	288.2	-	-	-	-
w3	-	-	-	2.158	2.239	2.381	-	-	-	-

Table S4. Fit Values used to fit detailed XPS spectra in the region of the Li 1s edge. The parameters represent: ai, area of peak i; pi, position of peak i; wi, FWHM of peak i.

	Li 1s									
	Diglyme 25 °C			Diglyme 50 °C			THF 40 °C			
	0 min	2 min	10 min	0 min	2 min	10 min	0 min	2 min	4 min	10 min
a1	4195	4421	4495	2060	2778	2880	3549	4147	4238	4483
p1	54.98	54.76	54.62	54.43	54.44	54.46	54.97	55.00	54.94	54.84
w1	2.237	2.286	2.270	2.173	2.131	2.161	2.372	2.157	2.153	2.173

Table S5. Fit Values used to fit detailed XPS spectra in the region of the O 1s edge. The parameters represent: ai, area of peak i; pi, position of peak i; wi, FWHM of peak i.

	O 1s									
	Diglyme 25 °C			Diglyme 50 °C			THF 40 °C			
	0 min	2 min	10 min	0 min	2 min	10 min	0 min	2 min	4 min	10 min
a1		868.4	6859	2.017E4	1.458E4	4.237E4	1.055E4	6408	5784	4222
p1	2.570	527.0	528.9	530.2	529.6	531.0	532.0	532.1	532.1	532.1
w1	5.400	1.300	1.875	2.200	2.298	2.601	2.694	2.856	2.856	2.856
a2	-	4114	3.651E4	3.032E4	3.753E4	7837	-	1800	2939	3762
p2	-	529.0	531.2	531.4	531.0	529.2	-	529.6	529.6	529.6
w2	-	1.738	2.975	2.600	2.568	1.995	-	2.746	2.777	2.777
a3	-	3.401E4	1190	-	-	392.5	-	296.1	479.0	725.5
p3	-	531.4	526.8	-	-	526.7	-	526.9	526.8	526.9
w3	-	2.95	1.213	-	-	1.113	-	1.324	1.555	1.885

Table S6. Summary of relevant literature binding energies

	C–C (eV)	C–O (eV)	C=O (eV)	O–H (eV)	Li–O (eV)	Li–F (eV)	B–F (eV)	B–O (eV)	B–C (eV)	B–B (eV)
O 1s	-	533[8]	532[8]	531[9]	528.5[9]	-	-	-	-	-
C 1s	284.8[10]	286.2[10]	289[11]	-		-	-	-	282.1	-
B 1s	-	-	-	-		-	194.8[12]	192[11]	188.4	187.4[13]
F 1s	-	-	-	-		684.8[14]	686.8[10]	-	-	

Figure S16. Changes to the Cu electrode during Li-N_2R

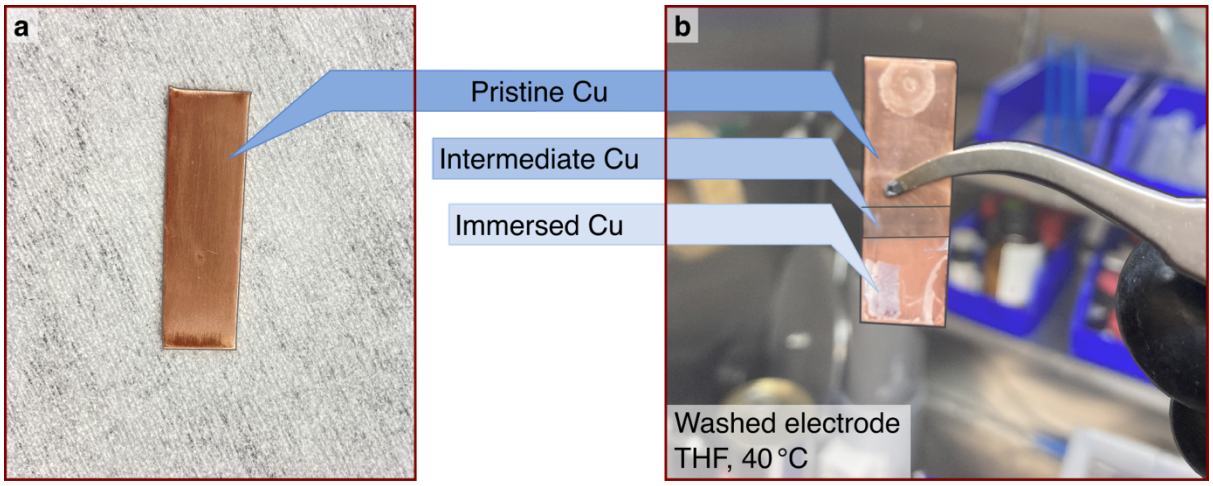

Figure S16. Evolution of the pristine copper electrode during Li-N_2R in THF-based electrolytes at 40 °C. While the pristine Cu electrode (a) is uniform throughout the entire electrode, three regions can be observed after Li-N_2R. At the top region, far away from the electrolyte, the Cu remains largely unaffected. The intermediate area of the electrode near the electrolyte surface was colored darker. Finally, the Cu electrode, visibly changes its color the moment it is immersed within the electrolyte, suggesting some form of etching.

Figure S17. ^{11}B NMR Spectra of the electrolyte after Li-N_2R reaction

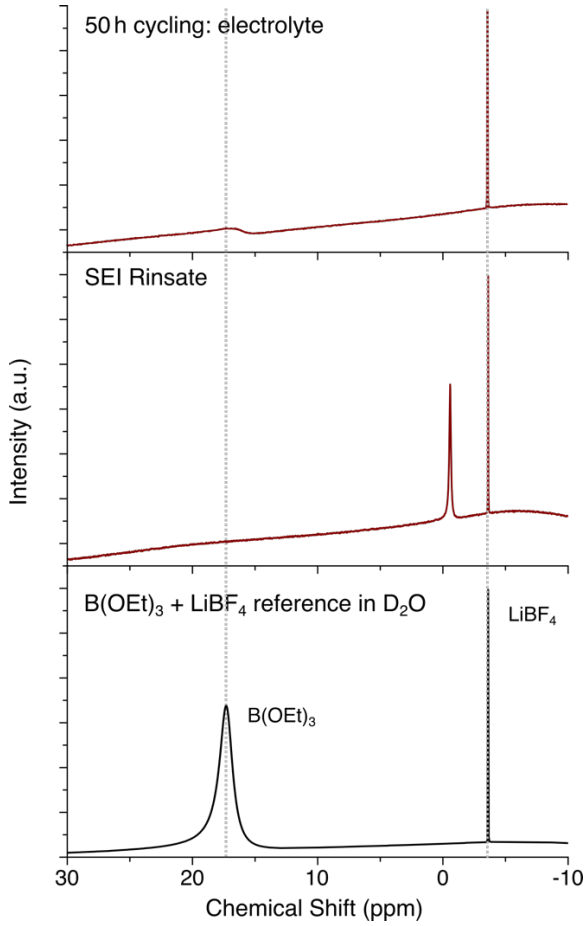

Figure S17. ^{11}B NMR Spectra of the electrolyte after Li-N_2R reaction at 50 °C in the electrolyte during long term cycling and in the rinsate after 16 mAh/cm^{-2} of passed charge. Both spectra are compared to a triethyl borate ($B(OEt)_3$) and a $LiBF_4$ standard. Apart from the LiBF4 signal that is visible in all samples, we observe a small broad peak in the range of the $B(OEt)_3$ peak that grows larger when the experiment is run extensively. Within the rinsate, we also observe an NMR peak in the range of 0 ppm that could arise from BF_3.[15,16]

Figure S18. All Li-N_2R Sampling runs with 0.33v % EtOH

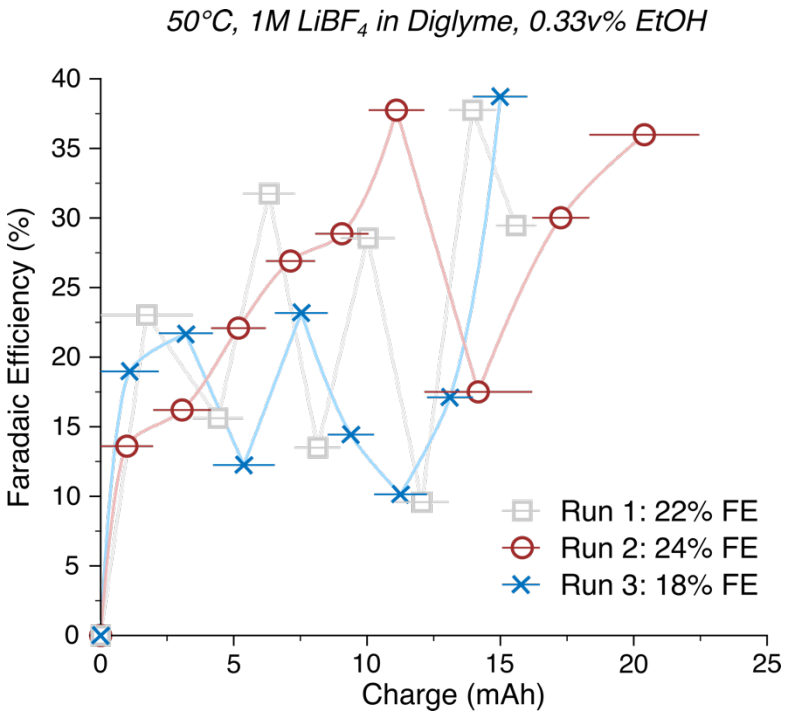

Figure S18. Summary of the temporal evolution of the Faradaic Efficiency (FE_{NH3}) at 50 °C with an EtOH content of 0.33 v%. Generally, the FE is increasing as a function of charge until drops of FE appear, likely due to delamination of the SEI from the Cu substrate. While the exact point of charge when delamination occurs is not always the same (as one would expect with the stochastic nature of delamination reactions that depend on substrate and SEI irregularities), the maximal FEs shown observed are all close 40 %.

Figure S19. Li-N_2R Control Runs

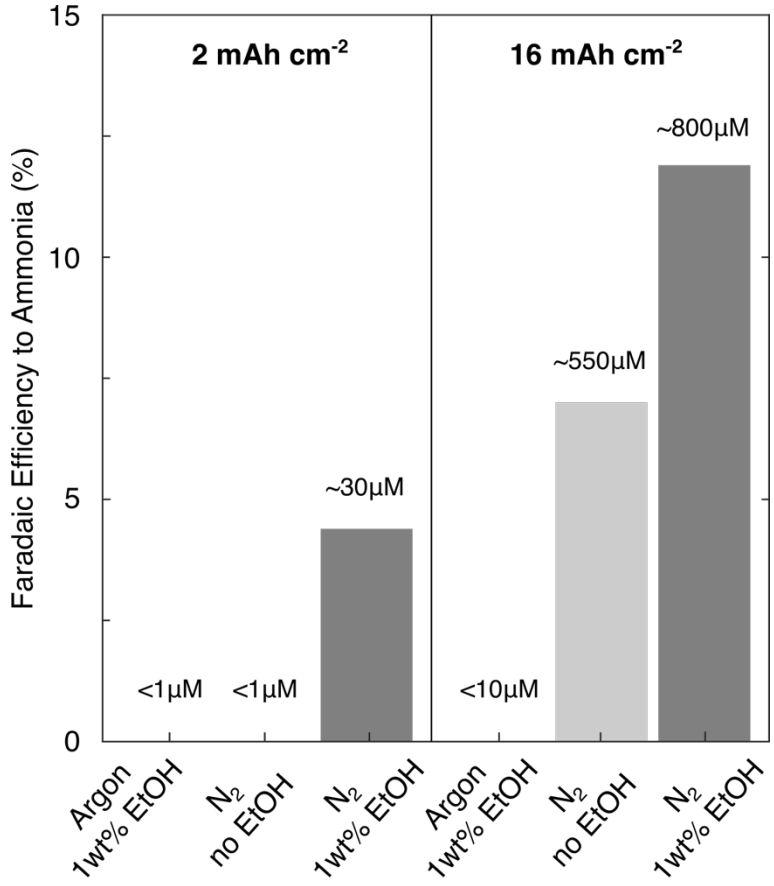

Figure S19. Control experiments of Li-N_2R runs in diglyme-based electrolytes. At 2 mAh cm^{-2} charge passed, we only observe a significant amount of NH_3 (> 5 μM) with N_2 and EtOH as proton source. At 16 mAh cm^{-2} charge passed, we do not observe NH_3 when Ar is sparged during the reaction. Without EtOH, approximately 550 μM of NH_3 was obtained, suggesting that protons obtained through diglyme oxidation were serving as the proton source for Li-N_2R to ammonia.

Table S7. Different Li-N_2R experiments in batch cells at ambient pressure

FE %	*Solvent*	*Salt*	*Charge (mAh/cm²)*	*Comments*	*Reference*
28	THF	$LiClO_4$	2.8	H_2O as additive	Spry et al.[17]
13	THF	$LiClO_4$	15.4	Current Cycling Approach	Zamany Andersen et al.[18]
17	THF	LiTFSI	~240	Constant Voltage experiments	Du et al.[19]
18	THF	$LiClO_4$	4	After Electrolyte Replacement	Valbæk Mygind et al.[20]
20	THF	$LiClO_4$	24	Additional H_2 bubbling	McShane et al.[21]
19	Diglyme	$LiBF_4$	16	Average FE	This Study
39	Diglyme	$LiBF_4$	11-15	Maximal FE	This Study

III. References

(1) McShane, E. J.; Benedek, P.; Niemann, V. A.; Blair, S. J.; Kamat, G. A.; Nielander, A. C.; Jaramillo, T. F.; Cargnello, M. A Versatile Li0.5FePO4 Reference Electrode for Nonaqueous Electrochemical Conversion Technologies. *ACS Energy Lett* **2023**, *8* (1), 230–235. https://doi.org/10.1021/acsenergylett.2c02190.

(2) Benedek, P.; Wenzler, N.; Yarema, M.; Wood, V. C. Low Temperature Hydrothermal Synthesis of Battery Grade Lithium Iron Phosphate. *RSC Adv* **2017**, *7* (29), 17763–17767. https://doi.org/10.1039/C7RA00463J.

(3) Li, S.; Zhou, Y.; Li, K.; Saccoccio, M.; Sažinas, R.; Andersen, S. Z.; Pedersen, J. B.; Fu, X.; Shadravan, V.; Chakraborty, D.; Kibsgaard, J.; Vesborg, P. C. K.; Nørskov, J. K.; Chorkendorff, I. Electrosynthesis of Ammonia with High Selectivity and High Rates via Engineering of the Solid-Electrolyte Interphase. *Joule* **2022**, *6* (9), 2083–2101. https://doi.org/10.1016/j.joule.2022.07.009.

(4) Nielander, A. C.; McEnaney, J. M.; Schwalbe, J. A.; Baker, J. G.; Blair, S. J.; Wang, L.; Pelton, J. G.; Andersen, S. Z.; Enemark-Rasmussen, K.; Čolić, V.; Yang, S.; Bent, S. F.; Cargnello, M.; Kibsgaard, J.; Vesborg, P. C. K.; Chorkendorff, I.; Jaramillo, T. F. A Versatile Method for Ammonia Detection in a Range of Relevant Electrolytes via Direct Nuclear Magnetic Resonance Techniques. *ACS Catal* **2019**, *9* (7), 5797–5802. https://doi.org/10.1021/acscatal.9b00358.

(5) Wang, C.; Gong, Y.; Dai, J.; Zhang, L.; Xie, H.; Pastel, G.; Liu, B.; Wachsman, E.; Wang, H.; Hu, L. In Situ Neutron Depth Profiling of Lithium Metal–Garnet Interfaces for Solid State Batteries. *J Am Chem Soc* **2017**, *139* (40), 14257–14264. https://doi.org/10.1021/jacs.7b07904.

(6) Deissler, N. H.; Mygind, J. B. V.; Li, K.; Niemann, V. A.; Benedek, P.; Vinci, V.; Li, S.; Fu, X.; Vesborg, P. C. K.; Jaramillo, T. F.; Kibsgaard, J.; Drnec, J.; Chorkendorff, I.

Operando Investigations of the Solid Electrolyte Interphase in the Lithium Mediated Nitrogen Reduction Reaction. *Energy Environ Sci* **2024**, *17* (10), 3482–3492. https://doi.org/10.1039/D3EE04235A.

(7) Seo, D. M.; Boyle, P. D.; Allen, J. L.; Han, S.-D.; Jónsson, E.; Johansson, P.; Henderson, W. A. Solvate Structures and Computational/Spectroscopic Characterization of LiBF4 Electrolytes. *The Journal of Physical Chemistry C* **2014**, *118* (32), 18377–18386. https://doi.org/10.1021/jp5046782.

(8) Younesi, R.; Hahlin, M.; Edström, K. Surface Characterization of the Carbon Cathode and the Lithium Anode of Li–O2 Batteries Using LiClO4 or LiBOB Salts. *ACS Appl Mater Interfaces* **2013**, *5* (4), 1333–1341. https://doi.org/10.1021/am3026129.

(9) Otto, S.-K.; Moryson, Y.; Krauskopf, T.; Peppler, K.; Sann, J.; Janek, J.; Henss, A. In-Depth Characterization of Lithium-Metal Surfaces with XPS and ToF-SIMS: Toward Better Understanding of the Passivation Layer. *Chemistry of Materials* **2021**, *33* (3), 859–867. https://doi.org/10.1021/acs.chemmater.0c03518.

(10) Qiao, L.; Cui, Z.; Chen, B.; Xu, G.; Zhang, Z.; Ma, J.; Du, H.; Liu, X.; Huang, S.; Tang, K.; Dong, S.; Zhou, X.; Cui, G. A Promising Bulky Anion Based Lithium Borate Salt for Lithium Metal Batteries. *Chem Sci* **2018**, *9* (14), 3451–3458. https://doi.org/10.1039/C8SC00041G.

(11) Zhou, H.; Xiao, K.; Li, J. Lithium Difluoro(Oxalate)Borate and LiBF4 Blend Salts Electrolyte for LiNi0.5Mn1.5O4 Cathode Material. *J Power Sources* **2016**, *302*, 274–282. https://doi.org/10.1016/j.jpowsour.2015.10.073.

(12) Liang, Y.; Kerr, R.; Wang, X.; Ueda, H.; Armand, M.; Forsyth, M.; Howlett, P. C. New Plastic Crystal Composite Electrodes Employing Delocalized Transition Metal Salts for Low-Cost, High-Safety All-Solid-State Salt Batteries. *Chemistry of Materials* **2024**. https://doi.org/10.1021/acs.chemmater.4c01003.

(13) Qiu, P.; Zhu, J.; Gao, S.; Zhang, S.; Gu, J.; Liu, F.; Guo, Z. Metal-Free Boron Catalyst with Oriented Crystal Phase Interfacial Interaction for Efficient Electrochemical Production of Hydrogen Peroxide. *J Mol Struct* **2023**, *1291*, 135971. https://doi.org/10.1016/j.molstruc.2023.135971.

(14) Yu, W.; Yu, Z.; Cui, Y.; Bao, Z. Degradation and Speciation of Li Salts during XPS Analysis for Battery Research. *ACS Energy Lett* **2022**, 3270–3275. https://doi.org/10.1021/acsenergylett.2c01587.

(15) Parimalam, B. S.; Lucht, B. L. Reduction Reactions of Electrolyte Salts for Lithium Ion Batteries: LiPF6, LiBF4, LiDFOB, LiBOB, and LiTFSI. *J Electrochem Soc* **2018**, *165* (2), A251. https://doi.org/10.1149/2.0901802jes.

(16) Eisele, L.; Laszczynski, N.; Görg, M.; Schneider, M.; Burger, S.; Radkte, V.; Lucht, B.; Krossing, I. Investigation of Mixtures of BF3 Carbonates and LiX (X = OCH2CF3, OC(H)(CF3)2, CO2CF3) as Novel Electrolyte Systems for Lithium Ion Batteries. *J Electrochem Soc* **2020**, *167* (8), 080507. https://doi.org/10.1149/1945-7111/ab8876.

(17) Spry, M.; Westhead, O.; Tort, R.; Moss, B.; Katayama, Y.; Titirici, M.-M.; Stephens, I. E. L.; Bagger, A. Water Increases the Faradaic Selectivity of Li-Mediated Nitrogen Reduction. *ACS Energy Lett* **2023**, *8* (2), 1230–1235. https://doi.org/10.1021/acsenergylett.2c02792.

(18) Andersen, S. Z.; Statt, M. J.; Bukas, V. J.; Shapel, S. G.; Pedersen, J. B.; Krempl, K.; Saccoccio, M.; Chakraborty, D.; Kibsgaard, J.; Vesborg, P. C. K.; Nørskov, J.; Chorkendorff, I. Increasing Stability, Efficiency, and Fundamental Understanding of Lithium-Mediated Electrochemical Nitrogen Reduction. *Energy Environ Sci* **2020**, *13* (11), 4291–4300. https://doi.org/10.1039/D0EE02246B.

(19) Du, H.-L.; Chatti, M.; Hodgetts, R. Y.; Cherepanov, P. V; Nguyen, C. K.; Matuszek, K.; MacFarlane, D. R.; Simonov, A. N. Electroreduction of Nitrogen with Almost 100%

Current-to-Ammonia Efficiency. *Nature* **2022**, *609* (7928), 722–727. https://doi.org/10.1038/s41586-022-05108-y.

(20) Valbæk Mygind, J. B.; Pedersen, J. B.; Li, K.; Deissler, N. H.; Saccoccio, M.; Fu, X.; Li, S.; Sažinas, R.; Andersen, S. Z.; Enemark-Rasmussen, K.; Vesborg, P. C. K.; Doganli-Kibsgaard, J.; Chorkendorff, I. Is Ethanol Essential for the Lithium-Mediated Nitrogen Reduction Reaction? *ChemSusChem* **2023**, *16* (22), e202301011. https://doi.org/10.1002/cssc.202301011.

(21) McShane, E. J.; Niemann, V. A.; Benedek, P.; Fu, X.; Nielander, A. C.; Chorkendorff, I.; Jaramillo, T. F.; Cargnello, M. Quantifying Influence of the Solid-Electrolyte Interphase in Ammonia Electrosynthesis. *ACS Energy Lett* **2023**, *8* (10), 4024–4032. https://doi.org/10.1021/acsenergylett.3c01534.